



NRC · CNRC

From Discovery to Innovation...

Concept Study of a Millimeter Camera for ALMA

Authors: Doug Henke, Stéphane Claude, and James Di Francesco

March 15, 2015

Version: A1

NRC Herzberg Astronomy & Astrophysics

5071 West Saanich Rd.
Victoria, BC, V9E 2E7
Canada

Contact: Doug.Henke@nrc-cnrc.gc.ca, James.DiFrancesco@nrc-cnrc.gc.ca



National Research
Council Canada

Conseil national
de recherches Canada

Canada

Table of Contents

1	Report Summary.....	6
2	Science Motivation.....	7
2.1	Background.....	7
2.2	Summary of HMBA's Worldwide.....	8
2.3	Modes of Operation.....	9
2.4	Complementarity of HMBA and ALMA Data.....	9
2.5	Requirements of New Instrument.....	10
3	Conceptual Design.....	11
3.1	Introduction.....	11
3.2	Dense Spacing of Detectors.....	12
3.3	Analogies from Incoherent Detectors and the Cold Stop.....	13
3.4	Consideration of PAFs.....	13
4	Analysis for a Fully Sampled DHA.....	14
4.1	Simplified Quasioptical Design.....	14
4.2	Feed Spacing and the Detector Array.....	15
4.3	Simplified GRASP Implementation.....	18
4.3.1	Optical Path and Detector Layout.....	18
4.3.2	Transmitted Radiation Patterns along the Optical Path.....	18
4.3.3	Aperture Efficiency at the Output of the Collimator.....	22
4.3.4	Cumulative Power Along the Transmitted Path.....	22
4.4	Summary for the Fully Sampled DHA.....	24
5	DHA with Twice-Nyquist Spacing.....	25
5.1	Variation of Spacing.....	25
6	Detailed Simulation of the Aperture Stop.....	31
6.1	Simulation Method.....	31
6.2	Exploration of Various Aperture Shapes.....	32
7	Compact 2SB Assembly for Twice-Nyquist Spacing.....	33
	Acknowledgment.....	36
	References.....	36

List of Figures

Fig. 1. (a) Example of a sparse hexagonal array (b) Successive pointings are shown	12
Fig. 2. Simplified unfolded optics demonstrating placement of cold stop.	14
Fig. 3. Examples of simple detector feeds for a dense array.	15
Fig. 4. S-parameters for the open waveguide and elliptical lens models.....	16
Fig. 5. Comparison of co-polar far-fields for the dense hexagonal array (DHA).....	17
Fig. 6. Simplified GRASP implementation for the DHA models shown in Fig. 3.....	18
Fig. 7. Co-polar radiation patterns, for an on-axis detector	19
Fig. 8. Co-polar far-field projections on-sky of each feed port	20
Fig. 9. -3 dB contours (FWHM) of the simulated co-polar far-field	21
Fig. 10. Effect of coupling loss	24
Fig. 11. Arrangement of a DHA with twice-Nyquist spacing	25
Fig. 12. Variation of DHA spacings.	26
Fig. 13. Corresponding lenses for each array of Fig. 12.....	26
Fig. 14. Co-polar far-field on-sky projections of each feed port using element spacings	27
Fig. 15. FWHM contours of the co-polar far-field on-sky projections.....	28
Fig. 16. Overall receiver noise for the DHA models shown in Fig. 12.	30
Fig. 17. Example of the CST model used to simulate the radiation pattern	31
Fig. 18. CAD models of aperture stops.....	32
Fig. 19. (a) Scale reference of twice-Nyquist (b) Open view of RF/LO combiner	33
Fig. 20. Integration of the combiner network for 2SB.....	34
Fig. 20. Full 2SB assembly for both polarisations.....	34
Fig. 21. Block implementation of the dual-linear 2SB assembly for machining.....	35
Fig. 22. Array implementation of the compact 2SB assembly	35

List of Tables

Table 1 Current or planned heterodyne multi-beam arrays (HMBA) on single-dish telescopes....	8
Table 2 Beam parameters as determined by fundamental mode quasioptics	15
Table 3 Calculated aperture efficiencies for the DHA models.	22
Table 4 Cumulative power along the optical path	23
Table 5 Comparison of system noise	24
Table 6 Cumulative power along the optical path.	29
Table 7 Comparison of system noise between a single-pixel receiver and a DHA element.	30

Acronyms

2SB	Sideband-Separating
ALMA	Atacama Large Millimeter/submillimeter Array
ASC	ALMA Sensitivity Calculator
CST	CST Microwave Studio (simulation software)
DHA	Dense Hexagonal Array
FoV	Field of View
FWHM	Full Width Half Maximum
HMBA	Heterodyne Multi-Beam Array
HPBW	Half Power Beam Width
GRASP	TICRA GRASP (simulation software)
IF	Intermediate Frequency
LO	Local Oscillator
NRC	National Research Council Canada
PAF	Phased Array Feed
RF	Radio Frequency
OMT	Orthomode Transducer
OTF	On-The-Fly
TPA	Total Power Array

1 Report Summary

The Atacama Large Millimeter/submillimeter Array (ALMA) is the premier instrument for observing the universe at millimeter and submillimeter wavelengths. Although ALMA is impressive in scope, ALMA's largest shortcoming remains its relative insensitivity to large-scale emission. Such emission can be critical to recover, so that accurate pictures are obtained of numerous, poorly understood astrophysical phenomena. Some measures are in place to allow such emission to be obtained, e.g., through the Total Power Array (TPA) antennas, yet these single-receiver facilities do not have the same intrinsic sensitivity of ALMA's array of fifty 12-m dishes (the 12-m Array).

Within this report, we propose a conceptual optical design for a receiver array intended for a TPA antenna to improve the mapping speed. The array requirements are heterodyne detection, dual-linear polarisation, and sideband-separating (2SB) receivers to maintain compatibility with the 12-m Array.

Our approach was to consider a densely packed heterodyne array and to apply the technique of a cold aperture stop that is used within incoherent, or direct detector, arrays. A conceptual design is applied to an ALMA 12-m telescope and the effect of detector spacing is explored. Using the radiation patterns of each array element, the truncated power by the cold absorbing stop can be reciprocally considered as a cold attenuator to the input of the receiver. In this way, the "cost" of closely spaced array elements can be quantified. Aperture efficiency of the telescope is also considered.

This report consists of the science background and motivation behind improving the TPA antenna mapping speed. A summary of existing heterodyne multiple-receiver instruments is provided and related to the requirements of a TPA antenna. Next, an optical design for a fully sampled hexagonally arranged array is presented. This extremely compact arrangement suffers from a very large increase in receiver noise. In the following section, the spacing is increased to "twice-Nyquist" (still very compact for heterodyne arrays) and a moderately sized array is shown to outperform a single-pixel receiver. A comparison is also made between sparse arrays and dense arrays and it is shown that comparative mapping speed between the two types of arrays is dependent on the ratio of receiver to system noise, e.g., it depends on how dominant the sky noise is compared to receiver noise. Within relatively high system noise conditions, a dense array will outperform a sparse array, but when the receiver noise dominates the system noise, a sparse array will likely be more efficient in mapping. Next, a more detailed modelling representation of the aperture stop is presented using a combination of CST and GRASP and the results show agreement with the preceding sections of the report. Finally, a compact sideband-separating arrangement (using a turnstile) is shown and then applied to an array spaced at twice-Nyquist.

Many system issues such as available interfaces, cryogenic cooling capacity, LO power, cabling, de-rotation, back-end requirements, and telescope slew rate have not been considered within this report and further study is required.

If the system noise conditions are preferable, using a twice-Nyquist dense hexagonal array (DHA) offers the benefits that four times as many elements may be imaged onto the focal plane and the number of pointings, to achieve full Nyquist sampling, is reduced to only four. The DHA may be implemented at any of the ALMA frequency bands, but it is shown that for the ALMA Band 3 frequencies, a "twice-Nyquist" DHA would perform similar to a sparse array at the mid-band, worse at the low-end, and better at the high-end. Accordingly, if there will be more observations using the TPA in the upper half of the band, a DHA would be favourable.

2 Science Motivation

2.1 Background

The Atacama Large Millimeter/submillimeter Array (ALMA) is the premier facility for observing frequencies at 84–950 GHz. ALMA consists of three arrays: i) a “12-m Array” of fifty 12-m diameter antennas that can be separated up to ~15 km for higher-resolution observations; ii) a “Compact Array” of twelve 7-m diameter antennas fixed to a maximum separation of 33 m for lower-resolution observations; and iii) a “Total Power Array” of four 12-m diameter antennas which provide single-dish data for post-reduction combination with interferometric data from the other arrays. The arrays are used separately, but the latter two are used exclusively to obtain data complementary to 12-m Array data. They are not used independently for large-scale surveys of millimeter/submillimeter emission. Each ALMA antenna is outfitted with a cryostat containing a suite of single-pixel receiver cartridges.

In this study, we explore a heterodyne multi-beam array (HMBA) instrument design for the ALMA Total Power Array antennas. An HMBA is, in general, an arrangement of multiple heterodyne receivers within a single telescope that allows for simultaneous observations of emission from several adjacent locations on the sky. HMBAs are now quite common instruments for single-dish millimeter/submillimeter telescopes, and are used for efficient mapping of line emission over wide fields of size many times their instantaneous on-sky footprints. In general, the larger the number of elements an HMBA has, the faster its wide-field mapping speed is.

Since ALMA’s Total Power Antennas are outfitted with single-pixel receivers, its ability to recover extended emission over wide fields is relatively limited. For example, 12-m Array observations can, on occasion, include observations of multiple adjacent pointings, i.e., “mosaics,” and certain projects may also require low spatial frequency (uv) data from the Compact and Total Power Arrays if the targeted emission is relatively extended. Of course, when needed, the Total Power Array antennas can observe the same area on the sky as the other Arrays do, one pointing at a time in succession, to acquire the needed single-dish data. Given the factor of 12.5 difference in total collecting area between the 12-m Array and the Total Power Array alone, it can be challenging to provide data from each array of similar sensitivity, though total power signals may themselves be intrinsically much brighter than the interferometric signals.

To improve the efficiency of the ALMA Total Power Array, HMBAs may be needed on its antennas. Acknowledging the complementarity of the Total Power Array to the 12-m Array, however, is key to designing an effective HMBA. For example, the 12-m Array could map fields of many square arcminutes in size (through hundreds of adjacent pointings) but it is likely impractical for it to map fields of many square degrees in size. Hence, an HMBA for a Total Power Array antenna does not need to have a large instantaneous on-sky footprint. In addition, an efficient HMBA should have a much more tightly packed arrangement of receivers than is the present norm of $\sim 2 \times \text{FWHM}$ of the beam. Such an arrangement would allow the recovery of Nyquist sampled, single-dish data of regions a few square arcminutes in size with a minimal number of pointings.

Table 1
Current or planned heterodyne multi-beam arrays (HMBA) on single-dish telescopes

HMBA	Host Telescope (Diameter in m)	Freq. Range (GHz)	No. Receiver Elements	Mid-Band On-Sky Spacing (arcsec)	Polarisation × No. Sidebands	Receiver Arrangement	Mid-Band Instantaneous Footprint Diameter (arcmin)
HARP	JCMT (15)	325-375	16	30	single × 1	4 × 4 (square)	2
SEQUOIA ¹	LMT (50)	85-116	16	24	single × 1	4 × 4 (square)	1.4
HERA	IRAM (30)	215-272	18	24	dual × 1	3 × 3 (square)	1
FOREST	Nobeyama (45)	80-116	4	51	single × 2	2 × 2 (square)	1.1
SUPERCAM	APEX (12)	329-360	64	36	single × 1	8 × 8 (square)	5.7
KFPA	GBT (100)	18-27.5	7	91	single × 2	1 × (1 + 6) (hexagonal)	3.6
ARGUS	GBT (100)	75-115.3	16	~15 ²	single × 1	4 × 4 (square)	
CHAMP+	APEX (12)	624-716, 785-935	2 × 7	19.2, 16.5	single × 1	2 × (1 + 6) (hexagon)	0.8, 0.7
LAsMA	APEX (12)	262-374	2 × 7	~16	single × 1	1 × (1 + 6) (hexagonal)	0.4
SSAR	Delingha/Nexans (13.7)	85-116	9	172	single × 1	3 × 3 (square)	6.6
CHAI	CCAT (25)	430-510, 800-835 ³	2 × 64	16.5 (460), 9.5 (806)	single × 1	2 × (8 × 8) ⁴ (square)	2.2 (460), 1.2 (806)

2.2 Summary of HMBAs Worldwide

To provide context for the HMBA design described in this document, Table 1 lists information on HMBAs at other observatories that are presently in operation or will soon be [1]–[12]. As noted earlier, HMBAs are now quite common and most single-dish submillimeter/millimeter facilities have at least one in their respective instrumental offerings.

Table 1 reveals that HMBAs exist, or are planned, at six frequency bands that ALMA can observe, i.e., 3, 6, 7, 8, 9, and 10. As far as we are aware, no HMBAs yet exist or are planned for ALMA Bands 1, 2, 4, or 5. Most HMBAs typically have ~10 receiver elements, though recent and future examples, SUPERCAM and CHAI, respectively, have considerably larger numbers

¹ SEQUOIA once consisted of two arrays of 16 receivers each with one array per polarization. One array will move to the 50-m Large Millimeter Telescope in Mexico while the other will move to the 14-m Taeduk Radio Astronomy Observatory in South Korea. The Table includes only the LMT version.

² S. Church, private communication.

³ CHAI will have a third array at 345 GHz that can replace either of the two higher frequency arrays as conditions warrant.

⁴ The CHAI baseline arrays have 64 receivers each but the goal is for CHAI to have arrays with 128 receivers each. The numbers provided in the Table are for the baseline arrays.

(64-128). HMBA receiver elements are typically placed in square configurations, e.g., 3×3 , but some have hexagonal configurations, e.g., $6 + 1$. All HMBAs have receiver elements that are as equally spaced from each other as possible. Older examples of HMBAs have receivers with SSB mixers while newer ones tend to have receivers with DSB, 2SB (single polarisation), or balanced mixers. Most HMBAs, except HERA and FOREST, detect a single polarization. Importantly, HMBAs share a design where the receiver elements have typical beam spacings of $\sim 2 \times$ FWHM. Depending on the element arrangement, the typical instantaneous on-sky footprint of an HMBA is typically a sparse sampling across a field-of-view $\sim 1\text{--}2$ arcminutes in diameter or more.

2.3 Modes of Operation

With several beams angularly and regularly distributed on the sky, HMBAs provide an efficient means for detecting extended astronomical emission. In cases of bright or very extended emission, HMBAs can be operated in “raster” or “daisy” modes where they are swept across areas much larger than their instantaneous footprints, obtaining, respectively, rectangular or circular maps with Nyquist spatial sampling, or better, using “On-The-Fly” (OTF) observing techniques. In cases of weaker or compact emission, HMBAs can be operated in a “jiggle” mode where they are effectively pointed at a regular series of angular offsets smaller than the angular separations of the beams on the sky, obtaining small maps the size of the HMBA footprint across with Nyquist spatial sampling. For the weakest emission, an HMBA can be operated in a “stare” mode with no offsets. With beam spacings typically $\sim 2 \times$ the beam FWHM, however, Nyquist sampling on the sky is not achieved with this mode. (In the presence of sky rotation, compensating optics, e.g., a K-mirror, can be included in the design to rotate the HMBA footprint and ensure stare-mode observations of fixed sky positions.)

2.4 Complementarity of HMBA and ALMA Data

Single-dish data complementary to ALMA 12-m and Compact Array data can be presently obtained from the single-pixel receivers on the TPA antennas or, perhaps, from HMBAs at other facilities. Here we examine current or planned HMBAs to see if such instruments can reasonably acquire such data. Note, however, that there may be logistic or programmatic difficulties associated with obtaining complementary data at other facilities.

To provide effective single-dish data for combination with mosaics, the single-dish observations need to include several on-sky positions sampled at Nyquist sampling or better to preserve all spatial scales from the single-dish beam size up to the size of the map. In addition, complementary data should be obtained with a single-dish telescope roughly twice the diameter of the individual antennas used to obtain the interferometer data, so that each dataset has a significant range of spatial frequency (uv) coverage in common, easing the combination of the different datasets. (We assume that similar *spectral* resolutions can be obtained from both the single-dish telescopes and ALMA.) Finally, an HMBA should be ideally located at a latitude similar to that of ALMA, so that no declination restrictions exist for acquiring complementary data. Further comments are given below.

Nyquist sampling: As described in section 2.3, HMBAs can be used in several ways to obtain maps of Nyquist sampling or better, and these data can be used in principle for combination with ALMA data. If single-dish data from previous programs do not already exist, e.g., from a line survey, such data may not be efficiently acquired by existing HMBAs. Briefly, since other facilities have HMBAs with receiver spacings of $\sim 2 \times$ the beam FWHM, it can be still observationally expensive to obtain the needed single-dish data. For example, raster or daisy

mode observations only efficiently cover areas much larger than the typical interferometer mosaic. Furthermore, though jiggle mode observations may provide data over smaller fields, such observations themselves may require significant investments of time to achieve Nyquist sampling of smaller fields. In addition, the instantaneous footprints of such instruments may be themselves too large for efficient acquisition of single-dish data, resulting in the acquisition of unneeded data at the map edge. HMBAs on the TPA antennas could in principle be optimized for complementarity with interferometers by having arrangements of receiver elements much more closely packed than other HMBAs.

Single-dish size: ALMA mosaic observations consist of 12-m Array data and when lower spatial frequency (uv) coverage is required, Compact Array mosaic data can be obtained. When even lower spatial frequency coverage is required over an extended area, at present, data from either multiple pointings of the single-pixel ALMA Total Power Array antennas or data from HMBAs from other observatories are obtained. As can be seen in Table 1, all HMBAs are on telescopes roughly twice the size of the 7-m Compact Array antennas, i.e., 12 m or larger. Hence, all HMBAs listed in Table 1 could conceivably provide complementary single-dish data for mosaics observed ALMA. In addition, HMBAs on the 12-m diameter Total Power Array antennas could also provide this function.

Latitude: Complementarity to ALMA observations also depends on availability of resources at various latitudes. FOREST, ARGUS, and SSAR, each at locations in the northern hemisphere, cover ALMA Band 3. HERA and HARP, in the northern hemisphere, and LAsMA and SUPERCAM, in the southern hemisphere, cover ALMA Bands 6 and 7, respectively. CHAMP+ and CHAI, in the southern hemisphere, cover ALMA Bands 9 and 10 and Bands 8 and 10, respectively. LAsMA, SUPERCAM, and CHAMP+ are located at APEX, adjacent to the ALMA site. CHAI will be located at CCAT, which will be also adjacent to the ALMA site. Hence, HMBAs at Bands 6, 7, 8, and 10 already exist in the southern hemisphere, at locations where they will be able to observe the same sky as ALMA. Note, however, that HMBAs at lower frequencies, i.e., ALMA Bands 3–6, are not available in the south. Nevertheless, FOREST, ARGUS, SSAR, and HERA will be able to cover significant fractions (50–70%) of the ALMA sky. Setting aside the above point about receiver element spacings, HMBAs designed for Bands 1–6 on the Total Power Array antennas themselves would therefore have no such declination restrictions in providing single-dish data for ALMA interferometric data.

2.5 Requirements of New Instrument

To maximize efficiency of Total Power Array observations of extended emission for combination with data from the 12-m and Compact Arrays, we propose the construction and installation of HMBAs on the TPA antennas. Here, we describe some requirements for such an instrument.

Size: At present, Total Power Array observations of extended emission are obtained through successive pointings of its single-pixel dual-polarization receivers. Given that there are four Total Power Array antennas, an HMBA installed on one TPA antenna (as a start) would need to have four dual-polarisation or eight single-polarisation receivers to obtain the same basic mapping speed (although the exact number depends on the map size, the spacing of the receiver elements, and their arrangement). To increase this mapping speed by a factor of 2, at least 16 single-pol receivers are needed.

Spacing and Arrangement: The HMBAs listed in Table 1 have typical beam spacings of roughly $2 \times \text{FWHM}$. At least Nyquist sampled single-dish data, however, are needed for

effective combination with interferometer data. Though such data could be acquired by these HMBA's through OTF or "jiggle" mode observing, each of these modes can be inefficient for producing maps that match the sizes of interferometer mosaics, since they may yield maps of area much larger than needed. Alternatively, an HMBA can be designed specifically for recovery of single-dish data by having a much more compact arrangement of receiver elements. For example, an HMBA with an on-sky beam separation at the angular scale required for Nyquist sampling would obtain the needed single-dish data with a single "stare" pointing of the array. Improvements could be realized even with a new HMBA with beam spacing greater than needed for Nyquist sampling but less than those of existing HMBA's. Larger maps can be made through successive pointings of the HMBA on the sky. Following these ideas, the ideal arrangement of receivers is not rectangular but rather hexagonal, as with interferometric mosaics, with the spacing between receivers again being much more closely packed than the existing HMBA's.

Band: Higher-frequency HMBA's may be considered preferable over lower-frequency ones because they maximize the efficiency of relatively scarce excellent weather conditions needed to observe at higher frequencies. Nevertheless, cost cannot be ignored and lower frequency HMBA's are likely easier and less expensive to build. Hence, a Band 3 HMBA may be the most promising option, at first. For example, a Band 3 HMBA could take the place of the Band 3 cartridge on one Total Power Array antenna, leaving three single-pixel Band 3 receivers available on the other antennas for single-pointing total power observations.

3 Conceptual Design

3.1 Introduction

An important figure of merit for a telescope is mapping speed, i.e., how much time is required to fully sample a given field of view. While single-pixel feeds may be designed to have high aperture efficiencies and excellent receiver sensitivity, in an effort to increase the mapping speed, arrays of detectors may be used to generate more simultaneous beams on sky (i.e., more pixels), at the cost of increased complexity and individual pixel performance degradation [1].

As an introduction, we first define what is meant by the terminology of full sampling with a dense hexagonal array (DHA) of coherent detectors. Coherence implies several things, one of which is that a single-mode detector is used [13]. Accordingly, the telescope is limited to a single spatial mode [14], [15], such that the received signal from a point source is a uniquely defined plane wave at the primary reflector rim and is ideally transformed to the focal plane with resolution limited by the Airy pattern. Of course, a strong motivator for coherent detection is that frequency resolution is preserved. To achieve full sampling, the array follows a hexagonal layout with Nyquist on-sky spacing. Finally, within this document, a multi-beam array refers to a single optical beam per detector element. In other words, it does not refer to a phased array feed (PAF) where one beam is synthesized using several elements.

We assume the important theorem of reciprocity in our analysis. As applied to an antenna, reciprocity implies that the received and transmitted radiation patterns are reciprocally identical for a given mode and polarisation as long as the antenna system is linear [16]. Reciprocity will be used to analyse the beam coupling to the telescope and also to evaluate the noise added to the receiver.

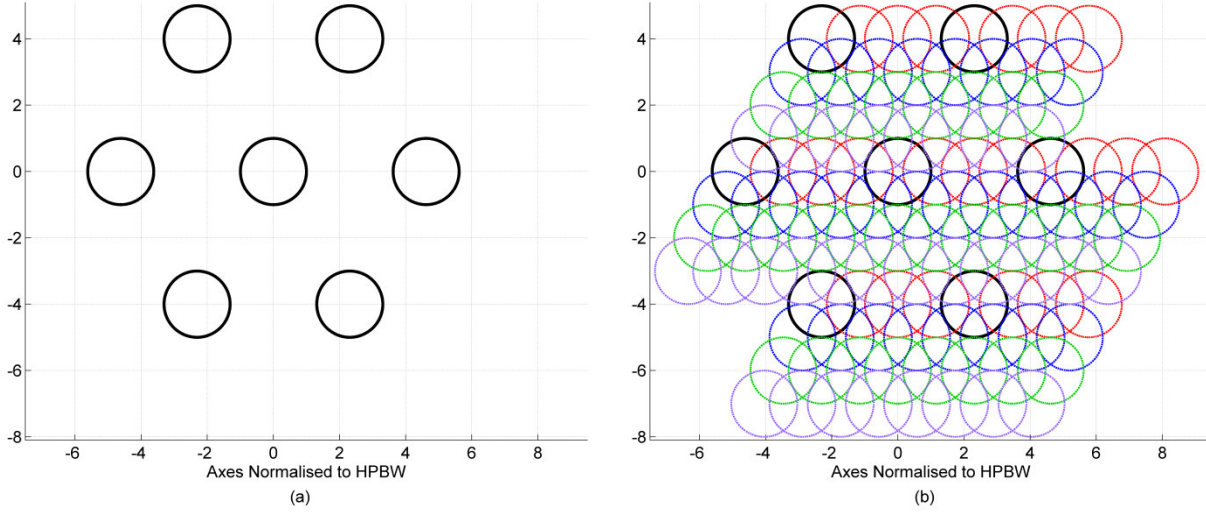


Fig. 1. (a) Example of a sparse hexagonal array (shown with the solid black circles) separated by $2 \times \text{FWHM}$. (b) Successive pointings are shown with dotted circles and each row contains four additional pointings, resulting in 16 total samples to fill the gaps within the map.

3.2 Dense Spacing of Detectors

To fully sample the field of view, Nyquist angular sampling must be achieved. Using a hexagonal layout, the angular on-sky sampling rate is

$$\Delta\theta_{\text{Nyq}} = \theta_{\text{FWHM}} / \sqrt{3} \approx \lambda / \sqrt{3} D \quad (1)$$

where λ is the wavelength and D is the diameter of the primary reflector [17]. When considering the focal plane of the telescope, the feed spacing is then

$$\Delta x_{\text{Nyq}} \approx \frac{\lambda}{\sqrt{3}} \frac{f}{D \cdot 1.2} = \Delta\theta_{\text{Nyq}} \frac{f}{1.2} \quad (2)$$

where f is the equivalent focal length of the telescope [17] and the additional factor of 1.2 is a spacing factor following [18]. Equations (1) and (2) are approximate since the -3 dB beam width, θ_{FWHM} , is assumed to be λ/D on-sky and $\lambda f/D$ at the focal plane.

Existing heterodyne arrays, like those of Table 1, are limited by the diameter of feed horn and the resulting element spacing is on the order of $\sim 2\theta_{\text{FWHM}}$ [19]. To obtain Nyquist sampling, the telescope is re-pointed many times to fill in extended fields of view due to the sparse sampling. Fig. 1 illustrates the additional sampling required for a sparse array such that when the frequency is chosen for horn spacing at exactly $2\theta_{\text{FWHM}}$, then 16 pointings are required to fill in the gaps within the map (when the spacing factor of (2) is set to 1.0).

Trade-offs must be made when increasing the density of the feeds within an array as two main problems are encountered: (a) possible mutual coupling effects and (b) severely reduced aperture efficiency through spill-over losses. Mutual coupling may be overcome by ensuring high isolation between feed ports. Spill-over, however, is a function of the aperture size. If the feed horn aperture is forced to be small to accommodate a closer packing density, the resulting beam will simply broaden with respect to the f/D of the telescope and be lost as spill-over power.

3.3 Analogies from Incoherent Detectors and the Cold Stop

There are analogies with efficiency and detector spacing for instrumentation design of infrared and optical incoherent detectors. For example, one could consider bolometric detectors and CCDs as suffering from a considerable amount of inherent spill-over, or stray light, but it is mitigated by the use of shrouds, baffles, and stops (see [24] as one example). Therefore, it is interesting to consider whether baffling and stops can be applied to coherent arrays.

We have used the following statement from [1] as motivation for our work:

Closer spacing is possible if the optical system uses more uniform aperture illumination with the detector beam truncated by a cold Lyot stop. This is a typical method for incoherent THz instruments but has not yet been implemented in a coherent array receiver.

In adopting these concepts for a millimeter-wavelength array, there are several questions. For example, what are the ideal qualities of the baffling and stop? What is the consequence of truncating the power? Where should the stop be placed? Can the receive and transmit paths of the signal be reconciled? What is the effect on the coherency of the signal?

We can philosophically address each of these questions. Baffling should be implemented so that the spill-over power gets absorbed without reflection to keep feeds isolated. Reciprocally, the termination can be thought of as noise power emitted into the receiver, so it is important that its physical temperature is some fraction of the equivalent receiver noise temperature. By making use of a collimator within the array, a stop may be placed at the point at which all beams coincide, i.e., the *optical waist*, such that each beam is truncated equally [25]. The stop needs to be evaluated (also using reciprocity) to analyse the characteristics of the diffracted beam through the stop and to calculate the resulting single mode aperture efficiency to validate the coherency of the detector. It is also useful to separate the spill-over power along the optical path into two contributions: (1) the spill-over power commonly associated with aperture efficiency which is evaluated at the sub-reflector of the telescope and (2) the power intercepted by the cold absorbing baffles and aperture stop.

3.4 Consideration of PAFs

Phased array feeds (PAF) may also be suitable for the TPA antennas. PAF technology has matured significantly over recent years, and provides an efficient means to form numerous beams on the sky with a much smaller instrumental “footprint” than sparse arrays described above. For example, this technology is currently being developed for the SKA in the 20 cm band [30]. These arrays have very large numbers (~100–200) of elements that sample the field-of-view through digital beam forming technology.

PAFs are very flexible and promising, but they do have added complexities over multi-beam arrays. For example, signal processing is very intensive for beam forming, mutual coupling between the feeds increases receiver noise, and element spacing is optimal for slower f/D of the telescope (since to minimise grating lobes, the element spacing should be $\lambda/2$ regardless of the f/D of the telescope).

For this study, we decided to concentrate on the possible application of a cold aperture stop with DHAs to provide a novel contribution with the additional intent that our study will complement PAF development.

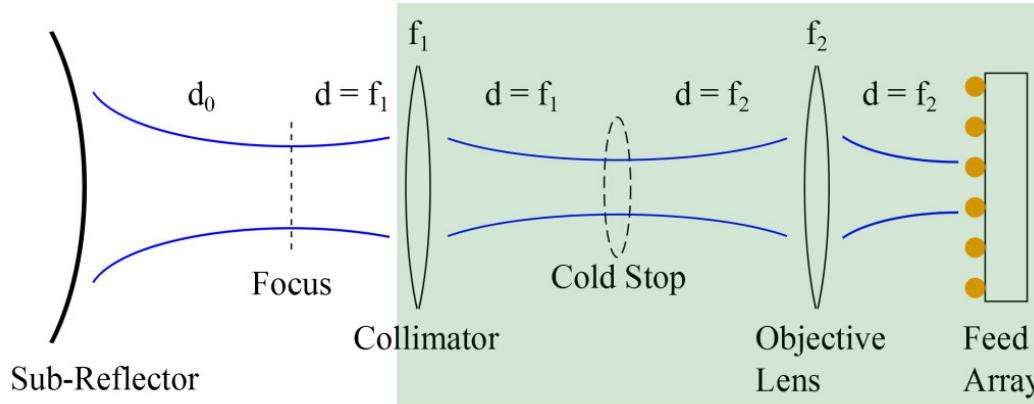


Fig. 2. Simplified unfolded optics demonstrating placement of cold stop. The shaded area represents the portion over which cold, absorbing baffling is used.

4 Analysis for a Fully Sampled DHA

Within this Section, the detector feed spacing has been chosen for full Nyquist sampling. In Section 5 wider spacing is considered.

4.1 Simplified Quasioptical Design

It is useful to consider the example frequency of ALMA Band 3 (84–116 GHz) to explore the impacts of a cold stop on a dense multi-beam array. A simplified example is shown in Fig. 2 where a collimator has been used after the telescope focus and then reimaged onto the detector array. It is assumed that the telescope $f/D = 8$ and the primary diameter is 12 m.

Baffling is indicated within the figure, shown by the shaded area, and represents the region over which any scattered power is terminated by absorber at cryogenic temperature. The beam outside of the shaded area is treated separately as aperture efficiency of the telescope (including its own spill-over efficiency term). To emphasize the point, the total spill-over of each detector has been divided into two parts: (a) scattered power between the collimator and detector, which is terminated by cryogenically cooled absorber, and (b) spill-over with respect to the sub-reflector of the telescope, which is included in the aperture efficiency term.

Using quasioptics [23], the ideal beam characteristics may be found by working backwards from the sub-reflector assuming that the edge taper and focus are constant over frequency when evaluated at the sub-reflector. Given the layout described in Fig. 2, the design is summarized in Table 2. In this design, the distance between the focal plane and sub-reflector is assumed to be 6 m and distances are given with respect to the focal plane in the direction towards the detector array. No truncation has been modelled within Table 2. Also, note that in these initial analyses, the diameter of the collimator is ~ 7 beam radii at the lowest frequency, implying that if the number of elements is increased to more than that shown in Fig. 3, the lens diameters will have to be increased.

Table 2
Beam parameters as determined by fundamental mode quasioptics

Frequency (GHz)	Sub-Reflector	Cassegrain Focus	Collimator Lens	Stop	Object Lens	Detector Array
Distances with respect to Focus (mm)						
84	-6000.0	0.0	157.8	315.6	473.4	631.2
100	-6000.0	0.0	157.8	315.6	473.4	631.2
116	-6000.0	0.0	157.8	315.6	473.4	631.2
Beam Radii (mm)						
84	319.0	21.4	23.5	8.41	22.4	21.4
100	319.0	17.9	20.2	8.40	19.4	17.9
116	319.0	15.5	18.0	8.40	17.2	15.5
Radii of Curvature (mm)						
84	-6000.0	6000.0	1051.4	-929.7	178.6	6000.0
100	-6000.0	6000.0	817.2	-1315.8	189.1	6000.0
116	-6000.0	6000.0	662.1	-1769.1	201.3	6000.0

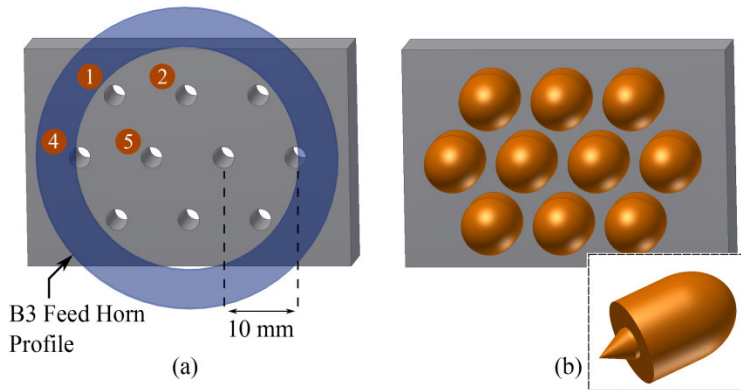


Fig. 3. Examples of simple detector feeds for a dense array: (a) circular waveguides, and (b) circular waveguides with extended elliptical lenses (inset). Each feed is arranged in a hexagonal layout and the circular waveguides are modelled within a simple metallic box. Simulation port numbers are indicated in (a) and represented by encircled numbers. Due to symmetry, it is sufficient to consider only ports 1, 2, 4, and 5. For comparison, the ALMA Band 3 receiver feed horn inner and outer profiles are shown to emphasize the compactness of the array element spacing.

4.2 Feed Spacing and the Detector Array

Next, it is important to consider what type of feed can be realized. To fully sample the field of view at the highest Band 3 frequency of 116 GHz, from (2) the spacing should be set at ~ 10 mm. Clearly there is no possibility to use an array of feed horns to achieve this compact spacing. For example, the current ALMA Band 3 receiver feed horn, shown for reference in Fig. 3, has an inner diameter of approximately 30 mm [26]!

Ideally, the array feeds should be simple, support dual linear polarization, and exhibit excellent port-to-port isolation. To demonstrate the importance of the feeds, two examples will be used for the dense hexagonal arrays (DHA). A simple array of circular waveguides, as shown in Fig. 3(a), could be used since they show good input reflection and isolation. To reduce the amount of power that is terminated with baffles and absorber, however, it is advantageous to try to increase the directivity of the beams. One simple method is to use an extended elliptical lens at the

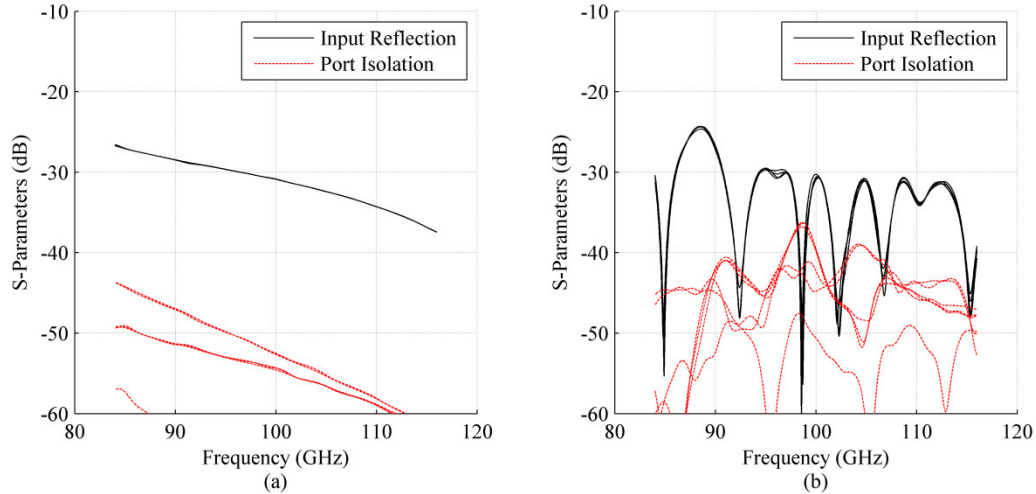


Fig. 4. S-parameters for the open waveguide and elliptical lens models shown in Fig. 3, (a) and (b) respectively, indicating the input port reflection (S_{11} , S_{22} , S_{44} , and S_{55}) and the port-to-port isolation (S_{21} , S_{54} , S_{41} , S_{52} , S_{51} , and S_{42}). Simulations completed using CST Microwave Studio. In both cases, port reflection is less than -20 dB and port-to-port isolation is less than -30 dB.

aperture [27] as shown in Fig. 3(b). The lens material⁵ is assumed to have a dielectric constant of $\epsilon_r = 1.93$ and is shown within the inset of Fig. 3(b). Since the lens has a low dielectric constant, no anti-reflection layer is required and a shallow input taper is used to improve input reflection. Fig. 4 indicates the suitability of each of the array feeds. Both are well matched across the band and display low levels of signal leakage between each feed port.

Fig. 5 demonstrates the difference in the far-fields of the feed arrays themselves when the extended elliptical lenses are used. In comparison to open-ended circular waveguides, the beams are narrower, more symmetric, and exhibit ~10 dB more gain. The added penalty, however, is an increased side-lobe value. For comparison, a single-pixel feed designed for the ALMA 12-m telescopes would have an opening half-angle of $\sim 3.5^\circ$. As such, both of the feeds shown in Fig. 5 are extremely broad and require careful attention to the spill-over power at each element along the optical path.

⁵ The example of Teflon® AF is used, although manufacturer data is only supplied at low frequencies.

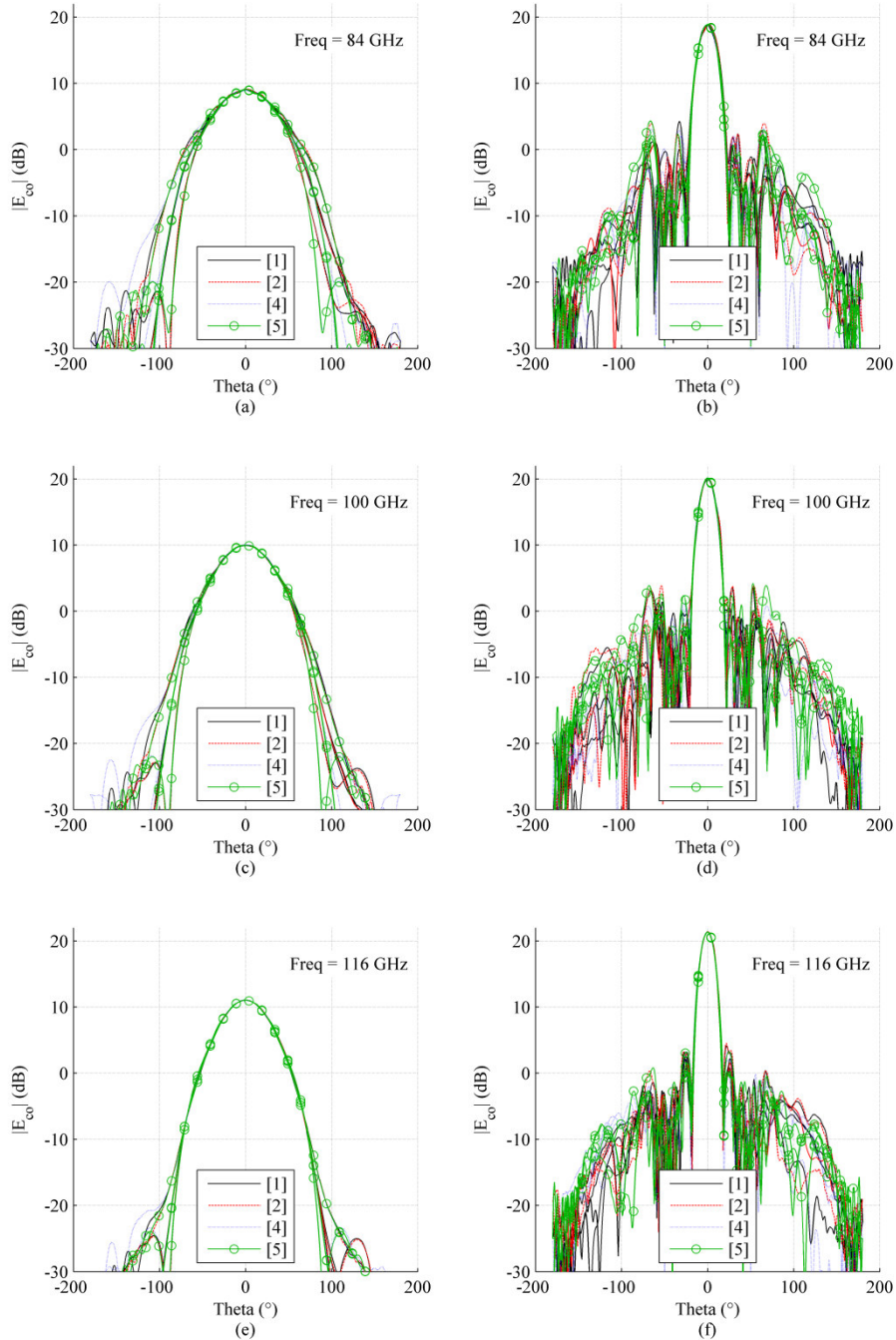


Fig. 5. Comparison of co-polar far-fields for the dense hexagonal array (DHA) models shown in Fig. 3. Left and right columns show the results from open-ended circular waveguides and extended elliptical lenses, respectively. Each plot contains the respective fields for ports 1, 2, 4, and 5 (labelled in brackets) and show field cuts overlapping at angles of $\phi = 0, 45, 90,$ and 135° . The beams are given for the frequencies of 84 GHz, 100 GHz, and 116 GHz, shown in (a)–(b), (c)–(d), and (e)–(f) respectively.

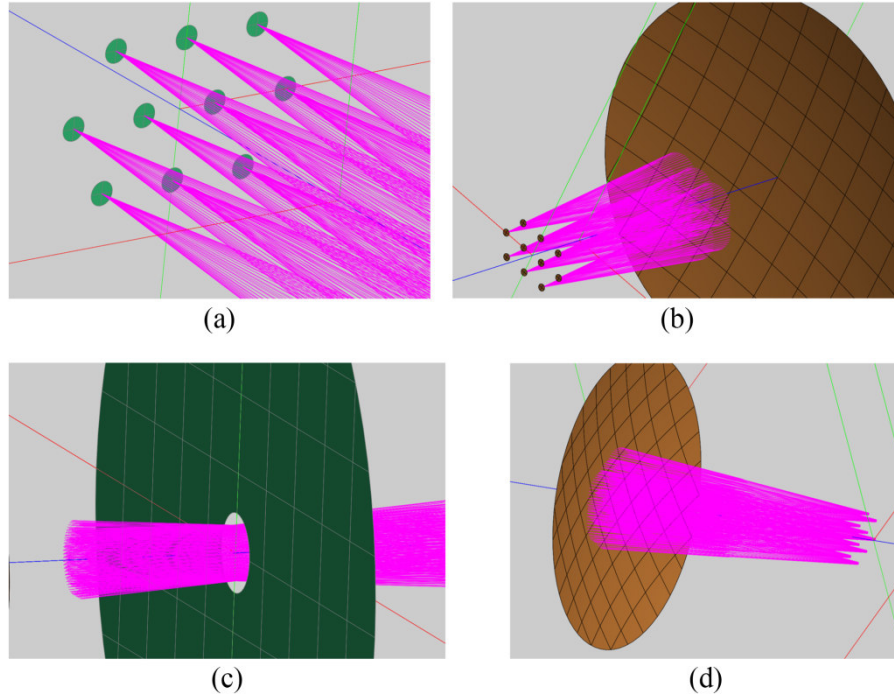


Fig. 6. Simplified GRASP implementation for the DHA models shown in Fig. 3. Each detector output has been represented by simple ray optics, using narrow beams for clarity. The layout follows the structure shown in Fig. 2 except the lenses are represented by reflectors and the beam is folded back. For clarity, the beams of the folded optics have been divided up to show: (a) the hexagonal layout of the detector feeds, (b) the off-axis beams illuminating the objective mirror and illustrating the size scale of reflectors, (c) the beams converging to share a common “optical waist” (coincident with the placement of the aperture stop), and (d) the output beams of the collimator to illustrate reimaging onto the focal plane.

4.3 Simplified GRASP Implementation

4.3.1 Optical Path and Detector Layout

As a first step towards verification, the dense hexagonal array (DHA) models of Fig. 3 were simulated using GRASP. In this preliminary approach, all the reflecting optics are placed on-axis and the unfolded optics, described in Fig. 2, are folded back along the axis (shadowing is not included in this simplified analysis). Fig. 6 describes the approach used. Although not shown, an equivalent paraboloid is used to represent an ALMA antenna with a focal length of 96 m and diameter of 12 m.

4.3.2 Transmitted Radiation Patterns along the Optical Path

Continuing with the transmitted path of the telescope (i.e., the detector array transmitting), an on-axis beam was evaluated at the different stages along the optical path and is plotted in Fig. 7 for the two types of feeds being considered. The aperture stop radius has been set to 11 mm (found to optimise the aperture efficiency) and is plotted with respect to a normalised feed power of 4π . As noted earlier, the gains are different between the feed types due to the focusing of the elliptical lens.

Several points of discussion follow from Fig. 7. First, the aperture stop, in (b) and (f), acts like a spatial filter resulting in a highly Gaussian distribution. Second, the output of the collimator, in (c) and (g), results in a radiation pattern that approaches a top-hat response; suggesting that the resulting beam may actually provide high aperture efficiency. Note that the

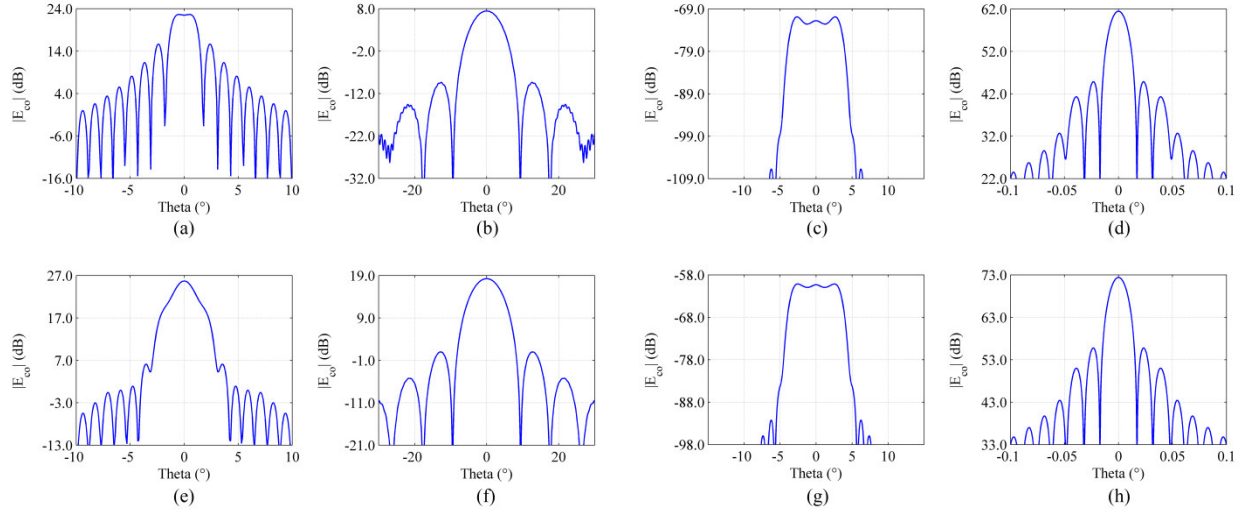


Fig. 7. Co-polar radiation patterns at 100 GHz, for an on-axis detector, after successive steps along the optical path for open waveguides (a)–(d) or extended elliptical lenses (e)–(h). The figures show: (a) and (e) the far-field after the objective mirror; (b) and (f) the far-field after passing through the aperture stop; (c) and (g) the near-field after the collimator and evaluated at the sub-reflector rim; and (d) and (h) the far-field after the telescope (equivalent paraboloid representation).

plots shown in (c) and (g) are near-field spherical data plotted with a reference distance of 6 m and with the origin at the focal plane to correspond to the field at the rim of the sub-reflector. Third, the far-field projections on sky show similar responses (except for gain) for both detectors.

Next, we consider the resulting far-fields of the telescope for the entire DHA. Fig. 8 shows the simulated co-polar far-field for each feed within the detector array when the extended elliptical lenses are used. Each subplot within the figure corresponds to the position of a feed element within the array. In Fig. 9, all simulated feed patterns have been plotted within the same u - v axes, but only showing the -3 dB contours for clarity. The FWHM contour circles correspond nicely with the expected spacing and show very dense spatial sampling. Since the spacing is set for the highest frequency, full sampling is observed at 116 GHz and oversampling at lower frequencies. Symmetry is evident and the resulting beams are encouraging since all beams are similar, indicating that the aperture stop is located properly and affects each feed element somewhat equally. When compared to open waveguides, adding the extended elliptical lenses helps in the resulting symmetry of the beams on sky.

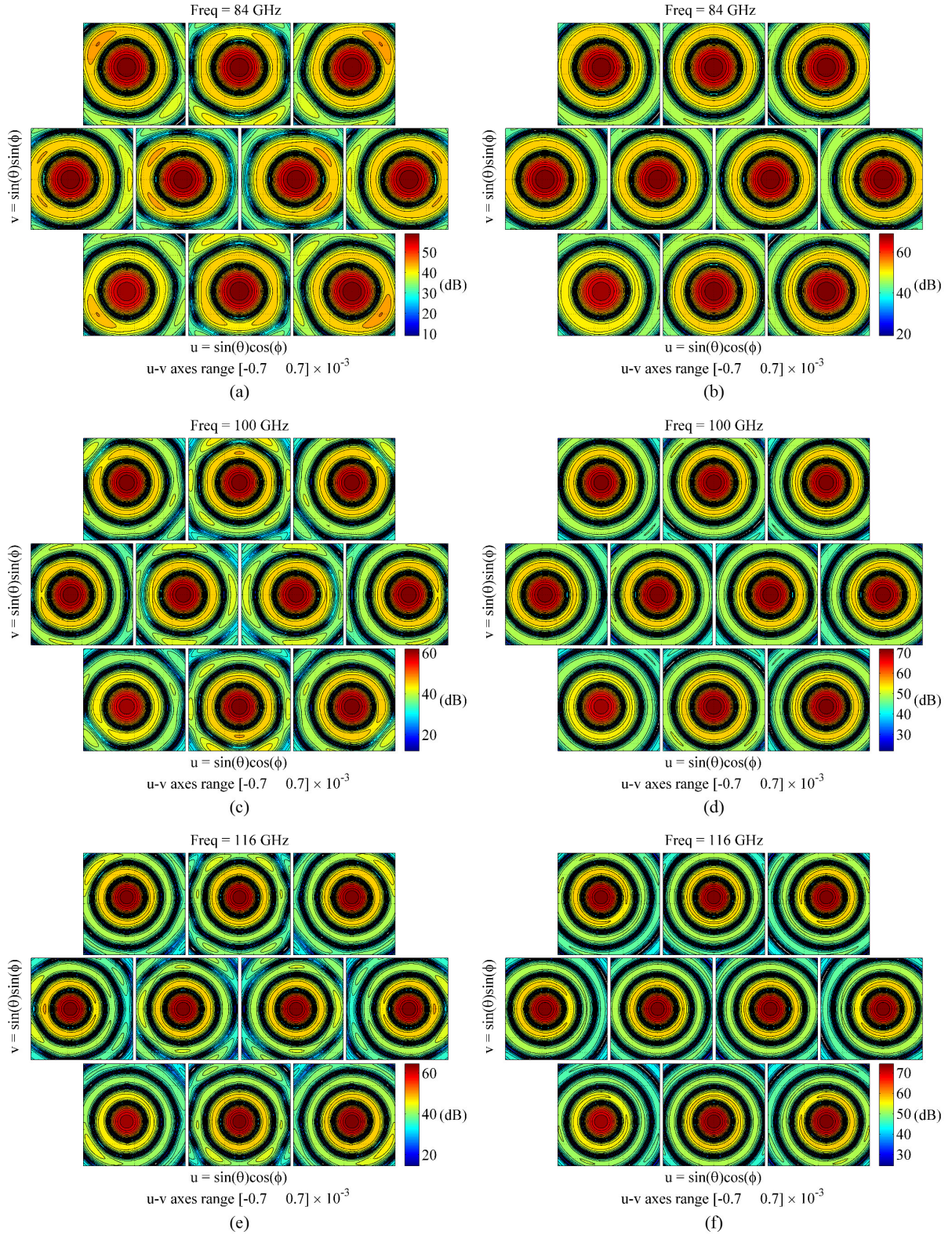


Fig. 8. Co-polar far-field projections on-sky of each feed port through the optical system (stop radius = 11 mm). Each beam is plotted separately, but shown in their respective position according to Fig. 3. The subplots on the left, (a), (c), and (e), are with the open waveguides, and the subplots on the right, (b), (d), and (f), are with the extended elliptical lenses. Both models are shown for 84 GHz, 100 GHz, and 116 GHz, respectively, in rows. Contour lines show 2 dB intervals and are plotted over a 50 dB range.

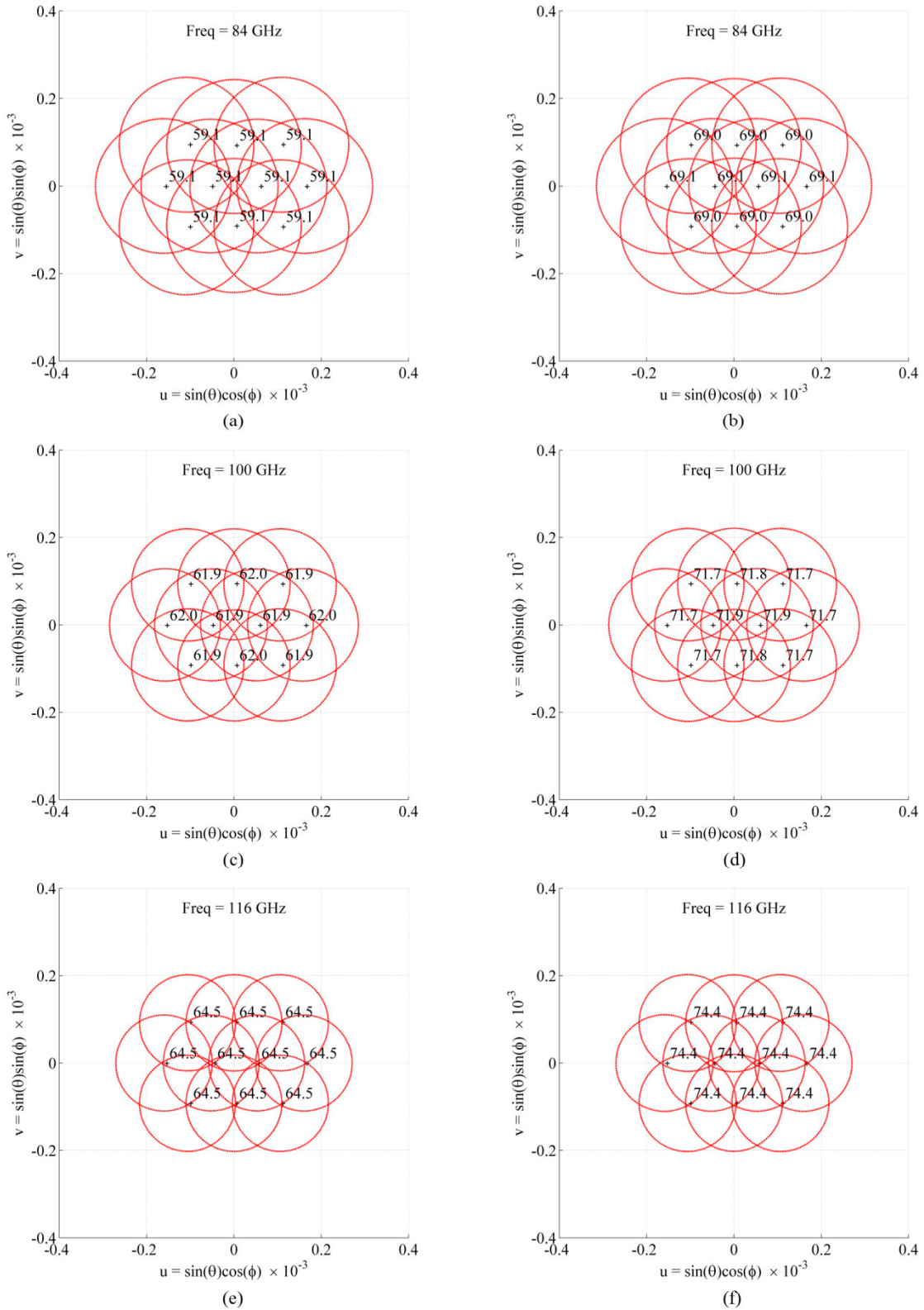


Fig. 9. -3 dB contours (FWHM) of the simulated co-polar far-field, as shown in Fig. 8, but plotted within the same axes. Peak values, given in dB and normalised with respect to each feed array element, are given for each beam.

Table 3

Calculated aperture efficiencies for the DHA models of Fig. 3(a) and (b) using the 4th feed port and an opening angle of 3.58°. Spherical near-field data with a reference distance of 6 m and an origin at the focal plane of the telescope have been used.

Aperture Efficiency Open Waveguides, dx = 10.0 mm						
Feed Element	η_{spill}	η_{amp}	η_{cross}	η_{phase}	η_{total}	Frequency
1	0.893	0.983	1.000	0.989	0.869	84 GHz
2	0.871	0.989	1.000	0.986	0.849	
4	0.893	0.983	1.000	0.989	0.868	
5	0.894	0.982	1.000	0.990	0.869	
1	0.885	0.992	1.000	0.987	0.867	
2	0.879	0.992	1.000	0.986	0.860	100 GHz
4	0.875	0.992	1.000	0.987	0.857	
5	0.884	0.990	1.000	0.984	0.862	
1	0.886	0.991	1.000	0.989	0.868	116 GHz
2	0.882	0.993	1.000	0.987	0.864	
4	0.884	0.992	1.000	0.990	0.868	
5	0.871	0.996	1.000	0.985	0.854	
1	0.885	0.992	1.000	0.990	0.874	
2	0.888	0.989	0.999	0.991	0.869	
4	0.893	0.986	1.000	0.993	0.874	
5	0.885	0.991	1.000	0.991	0.870	
1	0.889	0.992	1.000	0.990	0.874	100 GHz
2	0.891	0.993	1.000	0.990	0.876	
4	0.890	0.992	1.000	0.991	0.875	
5	0.892	0.993	1.000	0.990	0.877	116 GHz
1	0.893	0.993	1.000	0.991	0.879	
2	0.890	0.995	1.000	0.990	0.877	
4	0.894	0.992	1.000	0.991	0.879	
5	0.889	0.995	1.000	0.989	0.875	

(a)

(b)

4.3.3 Aperture Efficiency at the Output of the Collimator

Next, it is useful to look at the resulting aperture efficiency of the output beam of the aperture stop. The aperture efficiency is calculated using an overlap integral [9], [17] at the rim of the sub-reflector with respect to the focal plane of the telescope. Note that the scattered or intercepted power between the feed array and collimator, i.e. within the cryostat, is not included within this calculation. Only the field at the sub-reflector rim is used and normalised accordingly. Given the simplifications of the model shown within this section, no back-scattering is included and the signal is assumed to be fully contained within θ ranging from 0–90°. Again, a stop aperture radius of 11 mm has been used. Table 3 contains the aperture efficiency calculations for each of the DHA models. The contributions of spill-over, amplitude, cross-polarisation, and phase efficiencies are shown. The resulting aperture efficiency for both DHA models is very good, with the important caveat that the truncated power between the collimator and the feed has not yet been accounted for.

4.3.4 Cumulative Power Along the Transmitted Path

Since we are using dense feeds with very broad radiation patterns, one main point of interest is how to treat the power that is truncated by the baffling and aperture stop. Using GRASP, the array feed element may be excited to calculate the amount of intercepted power within the shaded region of Fig. 2. The intercepted power is also, by reciprocity, the amount of power coupled into the detector with respect to the beam received at the collimator.

Table 4 shows the amount of power intercepted by each object along the optical path, as described in Figs. 2 and 6, when the radius of the aperture stop is 11 mm. For comparison, 100 GHz is used. Considering first the open-ended waveguides, (a), only ~43% of the power is intercepted by the objective lens. Then, most of the remaining power is absorbed at the cold stop so that only ~1% of the overall power actually arrives at the collimator mirror. Looking next at the elliptical lenses, (b), significantly more power is retained through the system, yet still only ~10% arrives at the collimator. We can also see that wider spacings relative to the frequency, correspond to more power at the collimator (i.e., the highest frequency has more cumulative power).

Table 4
Cumulative power along the optical path for the models of Fig. 3(a) and 3(b), using the 4th feed element and calculated for 100 GHz.

Cumulative Power (%) Open Waveguides, dx = 10 mm						Cumulative Power (%) Ellpt. Lens, dx = 10 mm					
Feed Element	Objective Mirror	Stop	Collimator	Equivalent Paraboloid	Frequency	Feed Element	Objective Mirror	Stop	Collimator	Equivalent Paraboloid	Frequency
1	34.4%	33.4%	0.8%	0.8%	84 GHz	1	77.8%	69.1%	8.1%	7.3%	84 GHz
2	34.6%	33.6%	0.8%	0.8%		2	76.0%	67.4%	8.0%	7.2%	
4	34.3%	33.3%	0.8%	0.8%		4	77.6%	68.8%	8.2%	7.4%	
5	34.8%	33.8%	0.8%	0.7%		5	73.8%	65.0%	8.1%	7.3%	
1	43.4%	42.1%	1.1%	1.0%	100 GHz	1	76.4%	65.3%	10.4%	9.5%	100 GHz
2	43.7%	42.4%	1.2%	1.0%		2	76.8%	65.5%	10.7%	9.7%	
4	43.2%	41.9%	1.1%	1.0%		4	77.1%	65.9%	10.5%	9.6%	
5	43.9%	42.6%	1.1%	1.0%		5	76.7%	65.0%	11.0%	10.0%	
1	53.2%	51.5%	1.5%	1.4%	116 GHz	1	82.2%	67.1%	14.4%	13.1%	116 GHz
2	53.7%	52.0%	1.5%	1.4%		2	82.6%	67.6%	14.3%	13.0%	
4	53.0%	51.3%	1.5%	1.3%		4	82.2%	67.2%	14.2%	12.9%	
5	53.9%	52.2%	1.5%	1.4%		5	82.3%	67.1%	14.5%	13.1%	

Herein lies the major hurdle towards acceptable performance for radio astronomy that the two feed models aptly illustrate. Since the assumption is made that the baffling and absorbing aperture stop are held at cryogenic temperatures, the optical coupling loss (i.e., the cumulative power received at the collimator shown in Table 4) may be effectively considered as a cold attenuator at the input of a receiver chain. Fig. 10 illustrates the consequence to overall receiver noise when the scattered power (i.e., power lost due to coupling losses) is terminated by the baffling at various physical temperatures. For illustration, it is assumed that the receiver element has an equivalent noise temperature of 35 K, representative of the ALMA Band 3 receiver cartridge [29]. By separating out the contribution of the power lost due to the baffling, two conclusions are shown: (a) the physical temperature of the absorber must be as cold as possible, and, (b) feed directivity is crucial. One can see that although both feed models provide good feed isolation and aperture efficiency outside of the cryostat, the coupling loss—even if the baffling is held at cryogenic temperatures—significantly degrades the resulting overall receiver temperature. In fact, the open-ended waveguides (coupling ≈ 0.01) result in an overall receiver noise that is off the chart in Fig. 10 and the extended elliptical lens array (coupling ≈ 0.11) shows a factor of ~ 10 degradation. One can also see that the power coupling changes significantly across frequency since the spacing has been fixed for 116 GHz.

To relate this degradation in terms of integration time, the system temperature must be known. From [18], neglecting background terms and pointing at zenith, the system temperature is

$$T_{sys} = \frac{1}{\eta_{eff} e^{-\tau_0}} (T_{rec} + \eta_{eff} T_{sky} + (1 - \eta_{eff}) T_{amb}) \quad (3)$$

where η_{eff} is the forward efficiency (fixed at 0.95 in [18]), $e^{-\tau_0}$ is the fractional transmission of the atmosphere, T_{sky} is the sky temperature, and T_{amb} is the ambient temperature (fixed at 270 K in [18]).

Using the ALMA Sensitivity Calculator (ASC)⁶, values of sky temperature and atmospheric transmission can be found and are shown in Table 5. Typical observing conditions are used for

⁶ <https://almascience.nrao.edu/proposing/sensitivity-calculator>

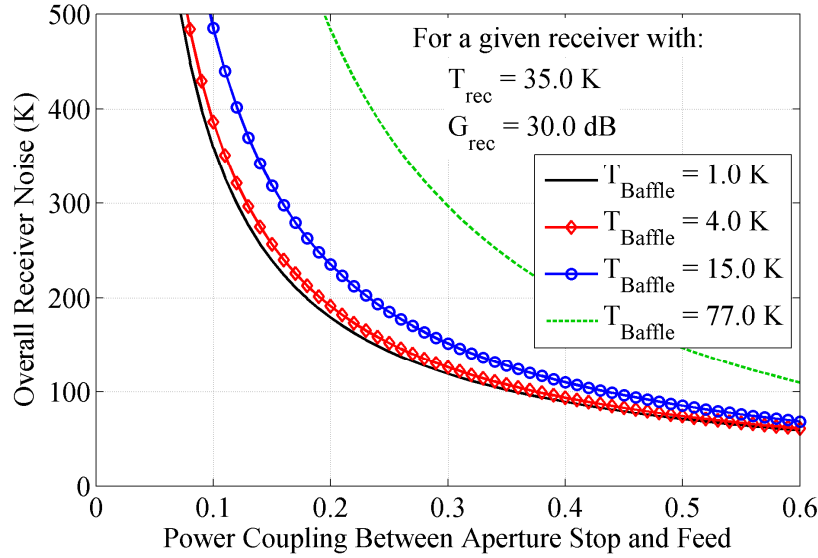


Fig. 10. Effect of coupling loss when the baffling structures, which terminate the lost power, are held at different physical temperatures.

Table 5
Comparison of system noise between a single-pixel receiver and an element within a fully sampled DHA with elliptical lenses (oversampled by a factor of 1.2).

Frequency (GHz)	τ_0	T_{sky}	Single Pixel		$\frac{\text{Nyquist}}{1.2}$	DHA	$(T_{\text{sys}} \text{ Ratio})^2 \leftrightarrow \tau_{\text{int}}$
			T_{rec}	T_{sys}	T_{rec}	T_{sys}	
84	0.048	12.924	35	67.1	483	561.9	70.1
100	0.054	14.196	35	68.9	368	438.8	40.6
116	0.336	69.531	35	168.7	275	522.3	9.6

ALMA Band 3, i.e., a water vapour column density of 5.1 mm is assumed. Also in Table 5, the last column shows the comparative increase in integration time between a single-pixel receiver and a DHA element (since integration time is proportional to the square of system noise temperature). Note that within the ALMA Band 3 frequency range, the upper frequency has considerably more atmospheric attenuation due to the water and oxygen absorption lines nearby. Since the sky noise temperature dominates the receiver noise temperature at the highest frequency, variations in receiver noise have less impact on overall system integration time.

Depending on how dominant the sky noise is, the number of fully sampled DHA elements using elliptical lenses ranges from ~10–70, just to have equivalent single-pixel performance.

4.4 Summary for the Fully Sampled DHA

An optical layout has been presented to explore the ramifications of full spatial sampling with multi-beam feeds using compact hexagonal spacing. Two different feed array models have been shown that exhibit the desired characteristics of simplicity, dual-linear polarization, good port match, high feed isolation, good aperture efficiency, and full Nyquist spatial sampling. The two models differ, however, in the amount of power lost in the cold baffling and absorbing aperture stop. By separately treating the scattered power between the aperture stop and feed array, the importance of feed directivity and absorber temperature are highlighted through representing the

coupling loss as cold attenuation at the receiver input. Since the feed aperture area fundamentally limits the directivity, extremely compact array spacings will suffer as shown above. The spacing presented within this section is extremely compact for coherent detectors, as the spacing was set for the highest frequency within the band, even with an additional spacing factor of 1.2 at the highest frequency.

Using a cold aperture stop also allows for wider spacings, still much more compact than existing heterodyne arrays, e.g., a spacing of $2\Delta x_{Nyq}$, and would imply only 4 separate telescope pointings to completely fill in the array field of view. Wider spacing would enable larger feed apertures (or larger lens diameters) to improve directivity of the beams and, therefore, shift the power coupling and drop the overall receiver noise, according to Fig. 10. This approach is considered in the following Section.

5 DHA with Twice-Nyquist Spacing

Following the same analyses as in Section 4, we will consider a DHA, but with wider spacings between detector elements. The goal is to see if higher optical coupling to the collimator can be achieved to shift the overall receiver noise according to Fig. 10.

Given the discussion above regarding sparse sampling (see Fig. 1), it is apparent that the number of separate telescope pointings can be reduced from 16 to 4 if the detectors have twice-Nyquist spacing, as shown in Fig. 11.

5.1 Variation of Spacing

Following Section 4, the same layout as Fig. 3 was kept, but the spacing between the elements was varied. The spacing factor of (2) was swept across values of 1.2, 1.0, 0.6, and 0.5, such that a factor of 1.0 and 0.5 correspond to Nyquist and twice-Nyquist sampling, set at the highest frequency of 116 GHz. The four models are illustrated in Fig. 12. For simplicity, the lenses of each array, shown in Fig. 13, were kept to have the same input circular waveguide and the lens diameter was set for $\Delta x_{Nyq} + 1$ mm. For each case, a single lens was optimised for beam quality and input reflection. Next, the entire array was simulated in CST Microwave Studio to ensure

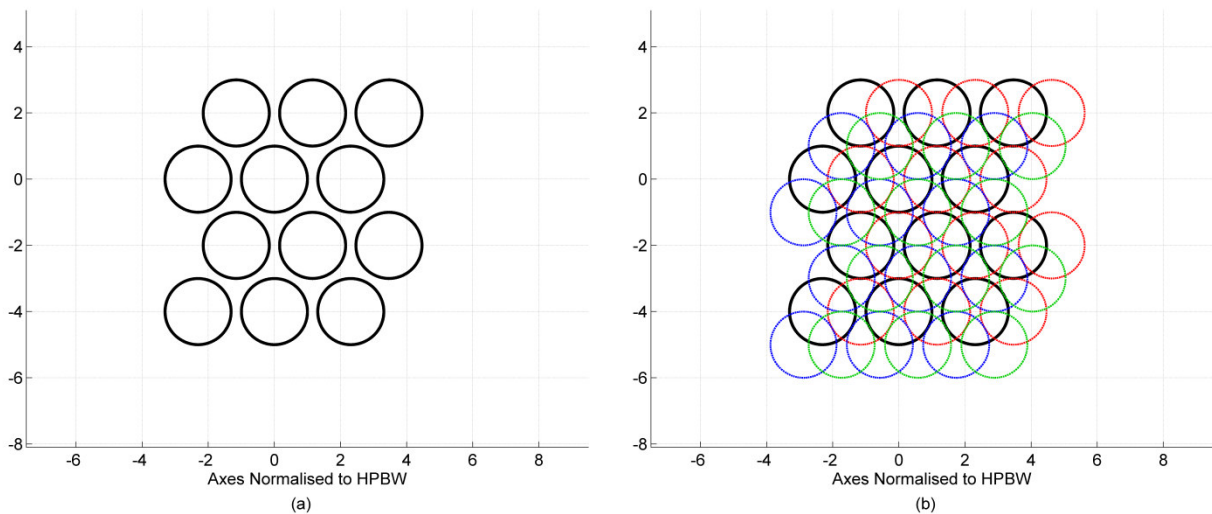


Fig. 11. (a) Arrangement of a DHA with twice-Nyquist spacing, shown here in a 4×3 layout. (b) Full sampling is achieved with only 4 separate pointings. Compare with Fig. 1.

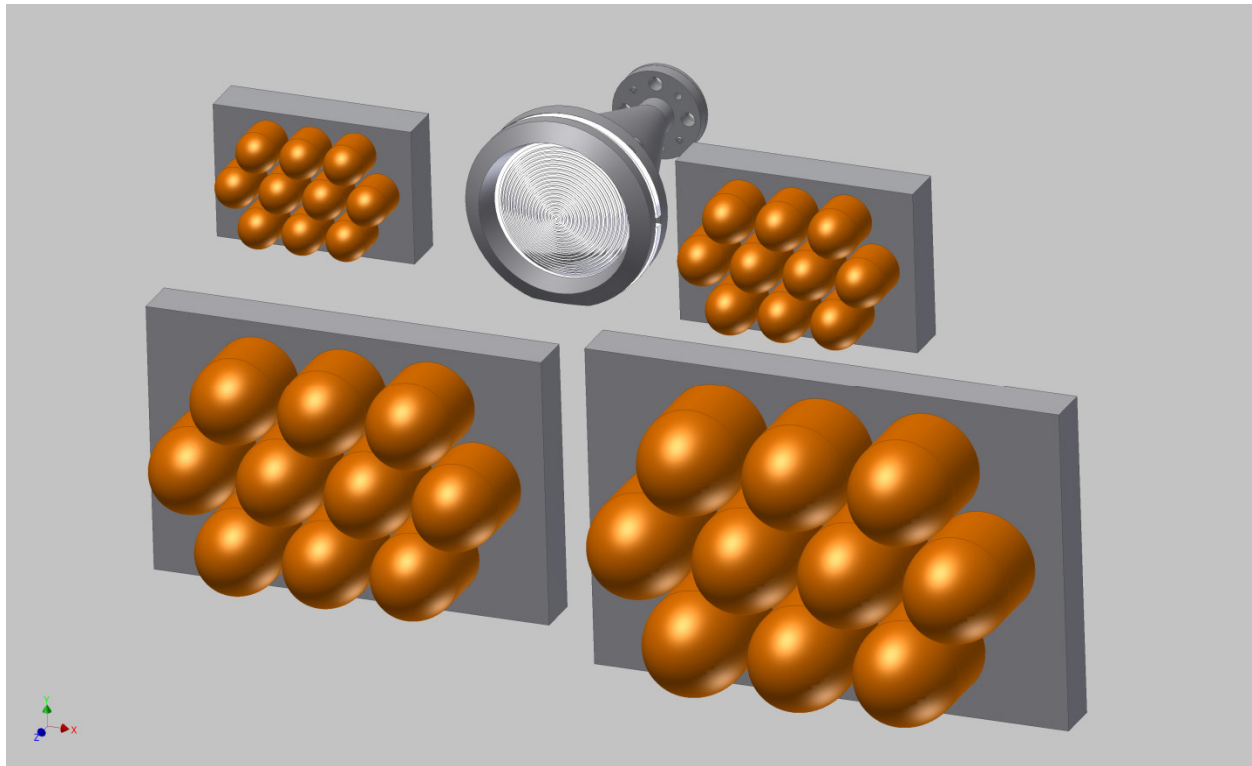


Fig. 12. Variation of DHA element spacing using spacing factors of 1.2, 1, 0.6, and 0.5, according to Equation (2). The two arrays on the right correspond to Nyquist and twice-Nyquist spacing. The ALMA Band 3 feed horn is shown in the upper middle for scaling reference.

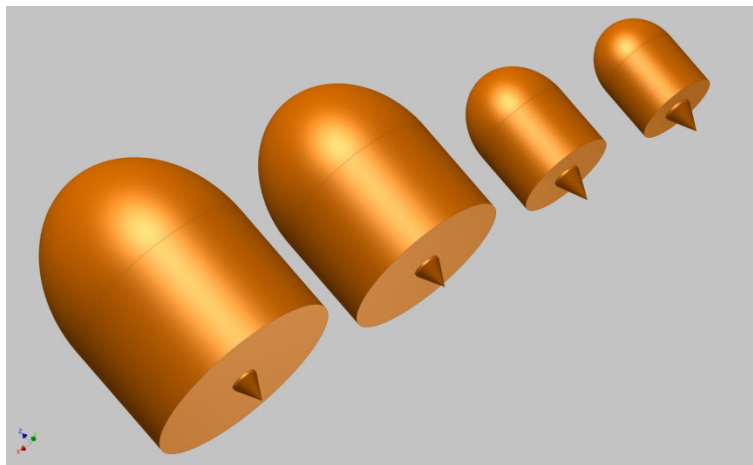


Fig. 13. Corresponding lenses for each array of Fig. 12. In each case, the same diameter of circular waveguide feeds the lens.

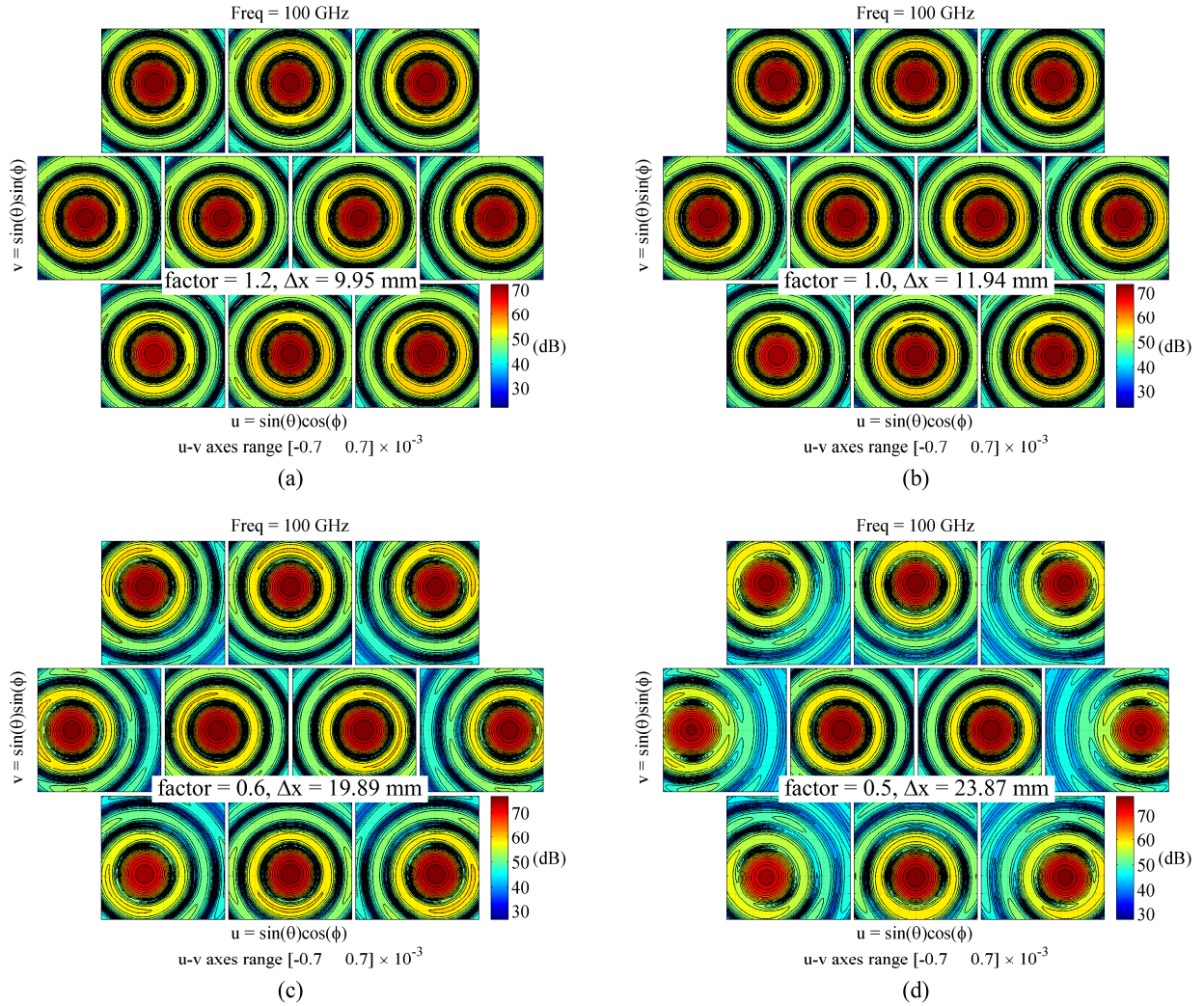


Fig. 14. Co-polar far-field on-sky projections of each feed port using element spacings corresponding to (a) slightly oversampled Nyquist, (b) Nyquist, (c) slightly oversampled twice-Nyquist, and (d) twice-Nyquist. The stop radius is 11 mm.

that port reflection < -20 dB and port isolation < -30 dB. Each port's near-field was exported to GRASP to analyse the optical path.

Fig. 14 compares the output far-fields of each array model at 100 GHz. As the spacing is increased to twice-Nyquist, shown in (d), the outer elements show some distortion of the beam. This distortion is likely due to the size of the optics in model (e.g., from Table 2, the diameter of the mirrors is ~ 7 beam radii at the lowest frequency). Even with the distortion, however, the calculated aperture efficiency for each case exceeds 80%.

Fig. 15 shows the simulated far-fields of each array model when the element feeds are plotted within the same axes. The FWHM contours at 116 GHz agree with the predicted spatial sampling.

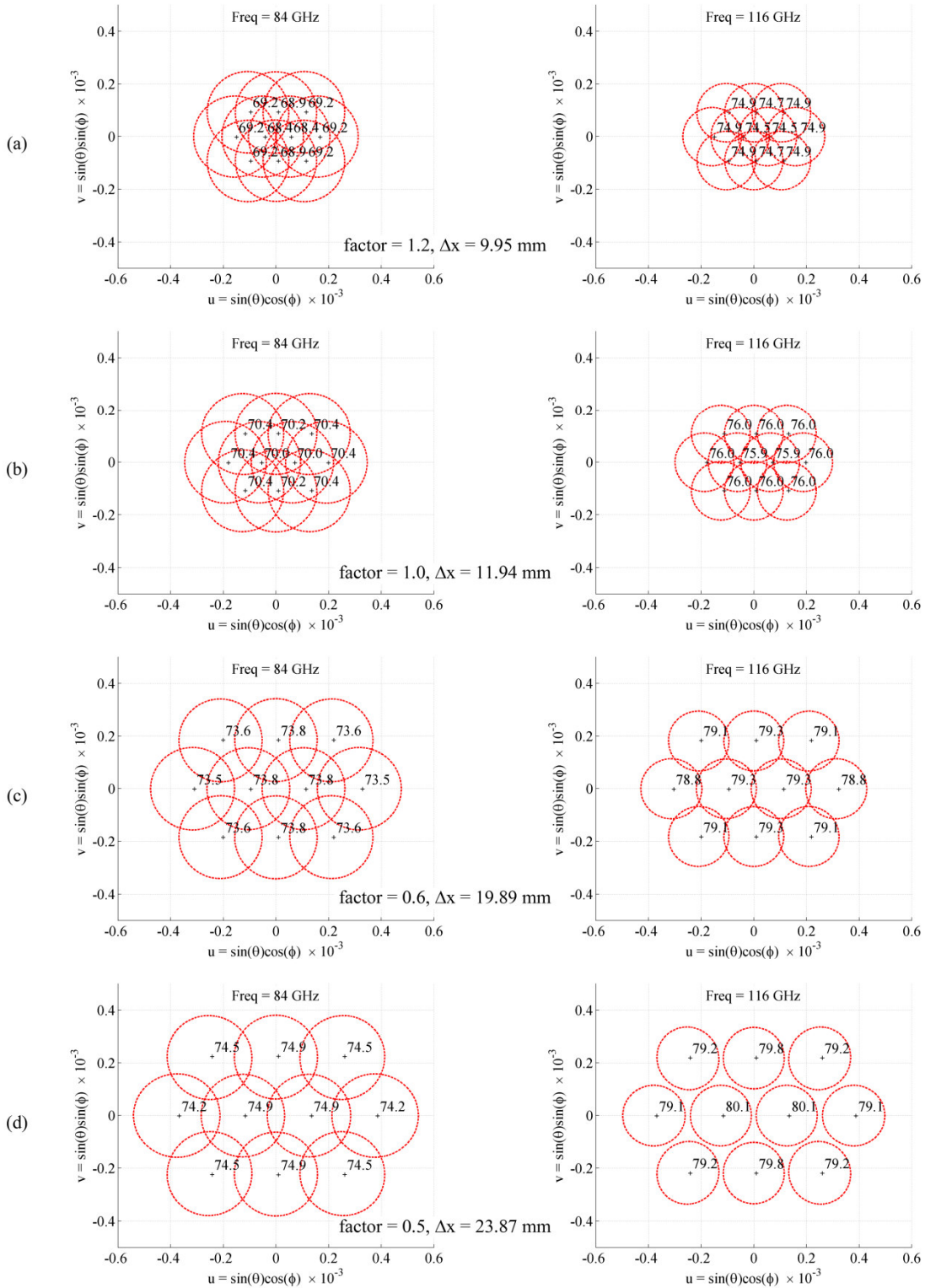


Fig. 15. FWHM contours of the co-polar far-field on-sky projections for each feed port using element spacings corresponding to (a) slightly oversampled Nyquist, (b) Nyquist, (c) slightly oversampled twice-Nyquist, and (d) twice-Nyquist.

Table 6
Cumulative power along the optical path for each array model with spacing: (a) slightly oversampled Nyquist, (b) Nyquist, (c) slightly oversampled twice-Nyquist, and (d) twice-Nyquist.

Cumulative Power (%)					
Ellpt Lens Dia = 8.95 mm, dx = 9.95 mm					
Feed Element	Objective Mirror	Stop	Collimator	Equivalent Paraboloid	Frequency
1	69.1%	60.0%	8.4%	7.6%	84 GHz
2	65.7%	57.3%	7.8%	7.1%	
4	69.3%	60.3%	8.3%	7.6%	
5	60.4%	53.0%	7.0%	6.3%	
1	75.6%	63.0%	11.9%	10.8%	100 GHz
2	74.8%	62.3%	11.7%	10.6%	
4	75.0%	62.7%	11.6%	10.5%	
5	71.8%	60.3%	10.8%	9.8%	
1	79.5%	62.7%	16.0%	14.6%	116 GHz
2	77.1%	60.8%	15.5%	14.1%	
4	79.7%	62.9%	16.1%	14.6%	
5	74.5%	59.0%	14.8%	13.5%	

(a)

Cumulative Power (%)					
Ellpt Lens Dia = 10.94 mm, dx = 11.94 mm					
Feed Element	Objective Mirror	Stop	Collimator	Equivalent Paraboloid	Frequency
1	66.8%	54.8%	11.1%	10.1%	84 GHz
2	65.4%	54.1%	10.5%	9.6%	
4	68.1%	56.2%	10.9%	9.9%	
5	60.9%	50.1%	10.1%	9.1%	
1	78.7%	61.9%	15.8%	14.4%	100 GHz
2	78.2%	61.5%	15.8%	14.4%	
4	78.3%	62.0%	15.4%	14.0%	
5	75.7%	59.8%	15.1%	13.7%	
1	83.3%	61.6%	20.7%	18.9%	116 GHz
2	83.5%	61.7%	20.9%	19.1%	
4	83.6%	62.0%	20.6%	18.8%	
5	80.4%	59.2%	20.4%	18.6%	

(b)

Cumulative Power (%)					
Ellpt Lens Dia = 18.9 mm, dx = 19.9 mm					
Feed Element	Objective Mirror	Stop	Collimator	Equivalent Paraboloid	Frequency
1	73.3%	48.4%	23.2%	21.3%	84 GHz
2	72.7%	47.3%	23.8%	21.9%	
4	72.7%	48.4%	22.6%	20.7%	
5	70.5%	45.1%	23.9%	21.9%	
1	77.9%	45.1%	31.1%	28.8%	100 GHz
2	76.7%	42.7%	32.4%	30.0%	
4	77.0%	45.0%	30.3%	28.1%	
5	74.2%	40.2%	32.6%	30.2%	
1	83.5%	39.7%	42.0%	39.0%	116 GHz
2	83.1%	37.6%	43.8%	40.8%	
4	82.7%	41.1%	39.7%	36.9%	
5	81.7%	36.3%	43.8%	40.7%	

(c)

Cumulative Power (%)					
Ellpt Lens Dia = 22.9 mm, dx = 23.9 mm					
Feed Element	Objective Mirror	Stop	Collimator	Equivalent Paraboloid	Frequency
1	70.4%	39.7%	28.7%	26.4%	84 GHz
2	68.8%	36.3%	30.6%	28.3%	
4	70.0%	40.6%	27.3%	25.0%	
5	67.6%	35.2%	30.6%	28.3%	
1	77.3%	39.2%	36.3%	33.7%	100 GHz
2	77.7%	35.8%	40.2%	37.4%	
4	77.2%	43.0%	32.1%	29.7%	
5	75.8%	32.2%	42.1%	39.3%	
1	82.2%	34.6%	45.7%	42.8%	116 GHz
2	81.5%	29.8%	50.1%	47.0%	
4	83.0%	37.2%	43.6%	40.6%	
5	81.8%	27.6%	52.7%	49.6%	

(d)

The change in power coupling is of interest for each case. Using the same methodology above, we assume the scattered power between the collimator and detector feeds is terminated by cold absorber. In the received path, the amount of power that is coupled into the detector with respect to the collimator is reciprocally identical to the simulated cumulative power at the collimator for the transmitted path. Table 6 summarises the cumulative power for each of the array spacings considered and shows significant improvement when using twice-Nyquist sampling, as in (d). Note that there is some variation in the results for the larger arrays, most likely due to the size of the optics and possible edge effects within the array. Increasing the size of the optics and adding a buffer ring of array elements terminated within the waveguide may mitigate these variations.

This interesting result may be quantified using the cold attenuator analogy described earlier. Fig. 16 shows the comparative overall receiver noise for each model. The shaded boxes within the Figure correspond to the range of optical coupling across the frequency band. For example, if Nyquist sampling is used, Table 6(b) shows that the coupling is ~10%, ~15%, and ~20% for each array element. This range of coupling is then mapped within Fig. 16(b) to illustrate that the overall receiver noise will range from over ~190–350 K, which results in receiver noise degradation factors of ~5–10 across the frequency band.

The amount of spread in the performance improves with twice-Nyquist spacing, shown in Fig. 16(d), changing the overall receiver noise to ~80–120 K, which is a factor of ~2.5–3.5 degradation.

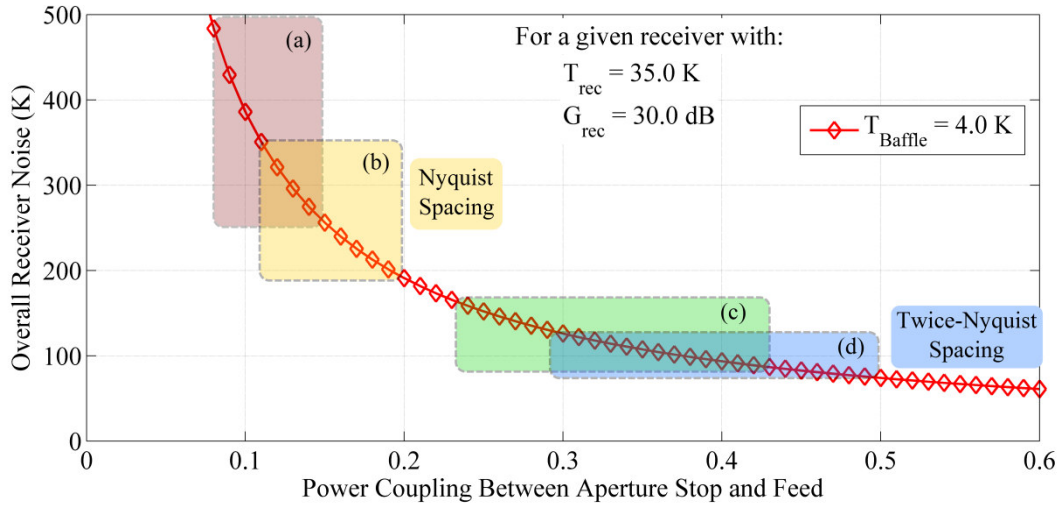


Fig. 16. Overall receiver noise for the DHA models shown in Fig. 12. The shaded boxes indicate the region of the curve that is covered across the frequency range of 84–116 GHz. It is assumed that the absorbed is held at a temperature of 4 °K.

Table 7
Comparison of system noise between a single-pixel receiver and an element within a twice-Nyquist DHA. Compare with Table 5.

Frequency (GHz)	τ_0	T_{sky}	Single Pixel		2 · Nyquist DHA		$(T_{\text{sys}} \text{ Ratio})^2 \leftrightarrow \tau_{\text{int}}$
			T_{rec}	T_{sys}	T_{rec}	T_{sys}	
84	0.048	12.924	35	67.1	130	172.0	6.6
100	0.054	14.196	35	68.9	94	134.4	3.8
116	0.336	69.531	35	168.7	74	226.2	1.8

As above, we can relate the change in receiver noise to the increase in integration time using (3). Assuming that aperture efficiency is constant, the integration time to achieve a given signal-to-noise is proportional to the squared system noise temperature, T_{sys} . In Table 7, the final column indicates the “break-even” point when comparing a DHA element with a single-pixel receiver. For example, at 100 GHz each element of the DHA requires ~4 times longer than an equivalent single-pixel receiver to achieve the same signal-to-noise.

As with all arrays, their mapping efficiency depends on the FoV observed. If the object can be characterised by only a few pointings of a single-pixel receiver, then arrays will not have any advantage. Of course, medium and large scales will benefit from more pixels as long as the resulting T_{sys} is not too adversely affected. For example, if a FoV as shown in Fig. 11(b) was required, then a single-pixel receiver would require 48 individual pointings to map the area. On the other hand, a 4×3 twice-Nyquist DHA at 100 GHz will need only 4 pointings, but each will take 4 times as long, resulting in an overall mapping efficiency improvement of a factor of 3. Larger DHAs will proportionately improve the mapping speed for larger FoVs.

It is also important to compare the DHA with a sparse array, i.e., compare Figs. 1 with 11. Here, we assume that a sparse array achieves 2-beamwidth spacing with no degradation in receiver noise temperature compared to a single-pixel receiver. The sparse array will always require a minimum of 16 pointings to fill in the gaps between pixels. Using Table 7, we can see that at 84 GHz, a sparse array is better (16 vs. 6.6×4), at 100 GHz, both arrays are similar

(16 vs. 3.8×4), and at 116 GHz, the DHA is better than a sparse array (16 vs. 1.8×4). Note that for a fair comparison, the sparse array should have its 2-beamwidth spacing set at the highest frequency (however, some sparse arrays achieve the 2-beamwidth spacing at mid-band).

Once again, the importance of the dominance of sky noise with respect to system noise is shown. The DHA is optimised within the upper part of the band (due to spacing) and is more efficient when the receiver noise, T_{rec} , is not the dominant term within the system noise, T_{sys} .

6 Detailed Simulation of the Aperture Stop

6.1 Simulation Method

Since simulation using physical optics is most suitable for electrically-large structures, and because the aperture is less than 10 wavelengths across, it was important to model the aperture with 3D electromagnetic simulation software to verify the diffraction through the stop. Modelling the entire optical path with CST's time domain solver is far too large for parameter sweeps and the approach was modified. First, the beam parameters were computed using quasioptics between the objective mirror and stop, assuming a transmitted path for a single on-axis DHA element. Then, a Gaussian excitation was used within CST to compute the near-field radiation pattern through the stop. Finally, the near-field data was imported back into GRASP and used to illuminate the collimator and simulate the telescope response (using an equivalent paraboloid representation of the telescope). Fig. 17(a) shows an example of the model used within CST and a Gaussian source excitation is shown behind the stop. The stop itself is comprised of a central metallic layer with two layers of absorbing material on each side⁷ for more realistic modelling (a close-up of the layers is shown in Fig. 18). For a cryogenic implementation, however, a ferrite-loaded epoxy may be more suitable. Note that the model of Fig. 17(a) is still electrically-large for a full-wave solver (~ 30 million cells) and a combination of CST and GRASP modelling is required to simulate the entire system.

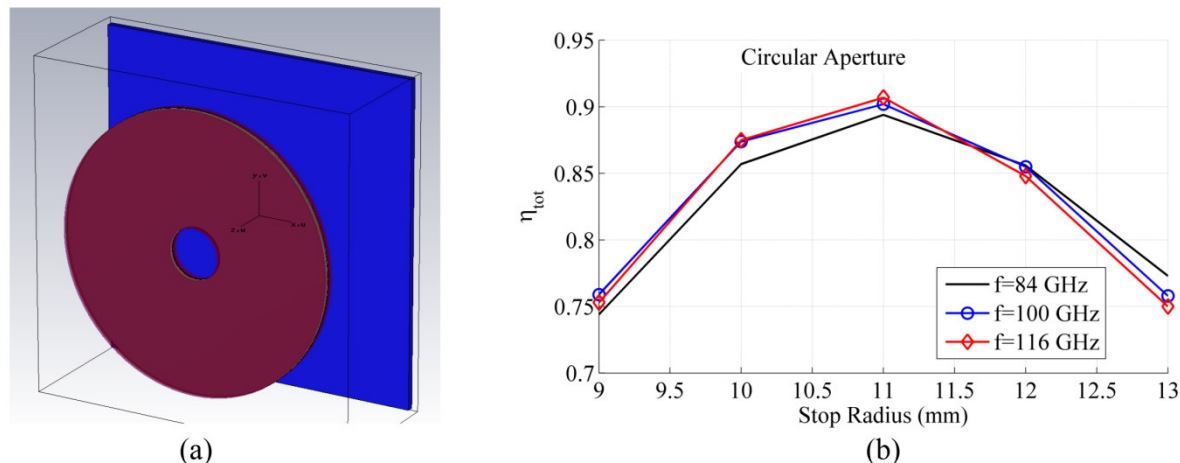


Fig. 17. (a) Example of the CST model used to simulate the radiation pattern through the aperture stop. The square blue feature in the back represents a Gaussian source with parameters determined by quasioptics. The aperture stop is modelled with a metallic plate and two layers of microwave absorber on each side. The near-field data is then exported into GRASP to calculate the aperture efficiency for various parameter sweeps, such as the stop radius shown in (b).

⁷ Absorber properties were modelled after ECCOSORB® MF110 and MF112.

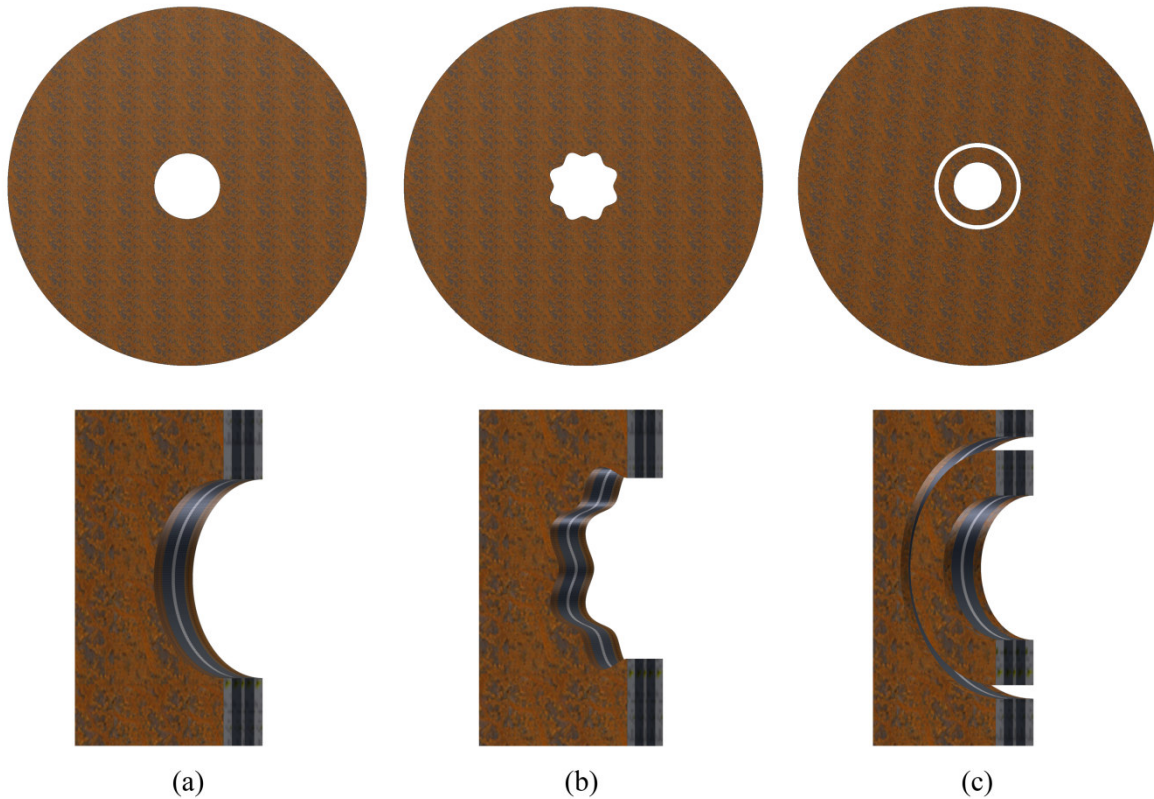


Fig. 18. CAD models of aperture stops used in full-wave modelling with CST Microwave Studio. (a) simple circular aperture, (b) sinusoidal aperture, and (c) circular aperture with an additional cut-out.

Once the near-field data is exported back into GRASP, the total aperture efficiency, η_{tot} , may be calculated following the same approach as in Section 4. Fig. 17(b) shows that the optimised stop radius for aperture efficiency for a simple circular aperture corresponds to 11 mm across the frequency band, which also agrees with the initial modelling using GRASP.

6.2 Exploration of Various Aperture Shapes

It is interesting to explore the impact of the aperture shape and Fig. 18 shows a sampling of some of the aperture shapes simulated. An empirical approach was used to run several parameter sweeps. For brevity, detailed results of the beams will not be shown. It suffices to say that, of all the experimental shapes, the simple circular aperture proved to give the best aperture efficiency and coupled power. One particularly interesting shape is shown in Fig. 18(b) because early simulations indicated a reduction in sidelobes of the radiated beam through the aperture. Upon further simulation with higher phi resolution, however, it was shown that the sidelobes increased with other phi cuts, resulting in no overall improvement.

7 Compact 2SB Assembly for Twice-Nyquist Spacing

If a compact element spacing such as that described here is adopted within an array, the next major challenge is to fit all of the receiver chain components within the volume. Retaining both linear polarisations and sideband-separation makes the problem even more challenging since for each feed element, four outputs are needed.

Fig. 19(a) shows the scale of the 2SB assemblies for the ALMA Band 3 receiver compared to the proposed twice-Nyquist element spacing. It is clear that for DHAs, the compactness of the following components needs to be improved by a factor of $\sim 10!$ Note that Fig. 19 does not show the down-converted IF part of each 2SB assembly. In Fig. 19(b), the assembly is shown open to indicate: (1) the 3 dB RF hybrid used to create a 90° phase shift between the RF branches, (2) the in-phase ‘Y-splitter’ used to divide the LO evenly between the branches, and (3) LO couplers preceding each mixer block [31]–[33]. Further details of sideband-separation can be found in [32].

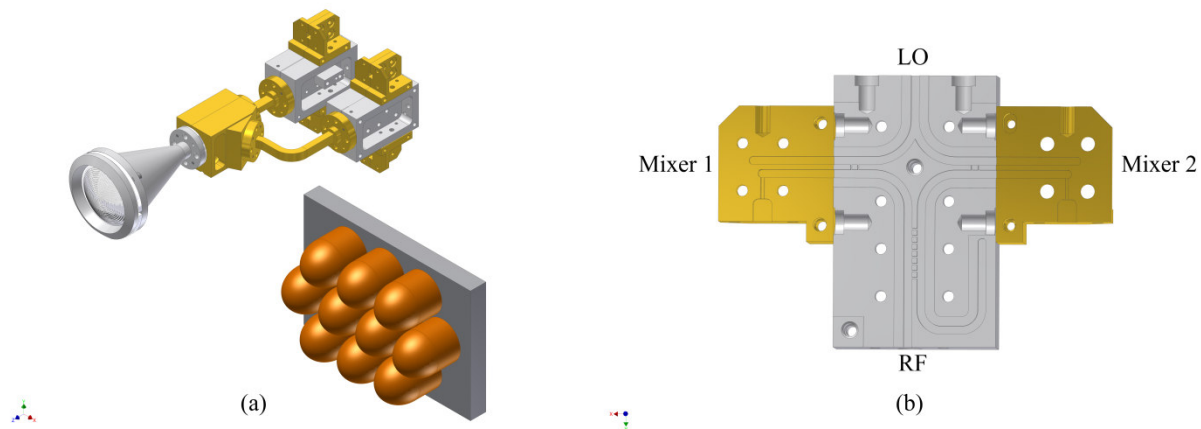


Fig. 19. (a) Scale reference between the twice-Nyquist spacing DHA model and a single ALMA Band 3 assembly for dual-linear and 2SB outputs. The 2SB assembly includes an OMT with each output attached to an RF/LO combiner network used in the sideband-separation. (b) Open view of the RF/LO combiner network with mixer blocks (coloured grey and gold respectively).

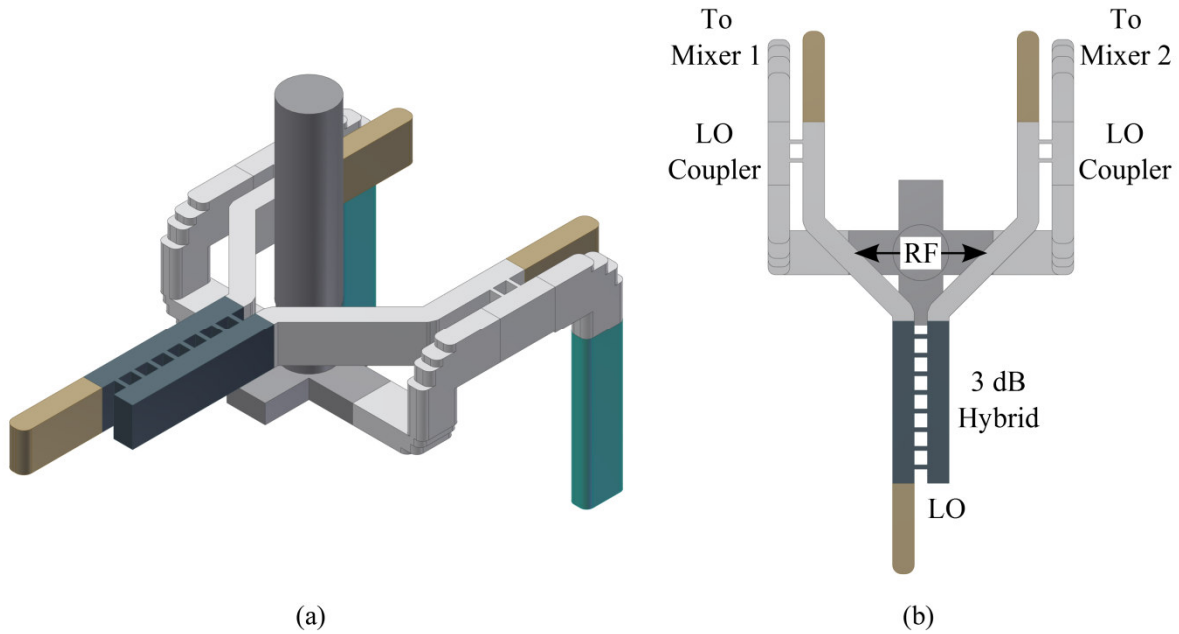


Fig. 20. Integration of the combiner network for 2SB, showing only the details for one polarisation, (a) isometric and (b) top views are shown. The RF signal is split in-phase via the turnstile and the LO is weakly coupled into each path. Before the LO is coupled, it undergoes a 90° phase shift with respect to its outputs via the 3dB hybrid. The RF + LO signal is then routed to a separate mixer block. The tan coloured waveguides are used to indicate a waveguide termination.

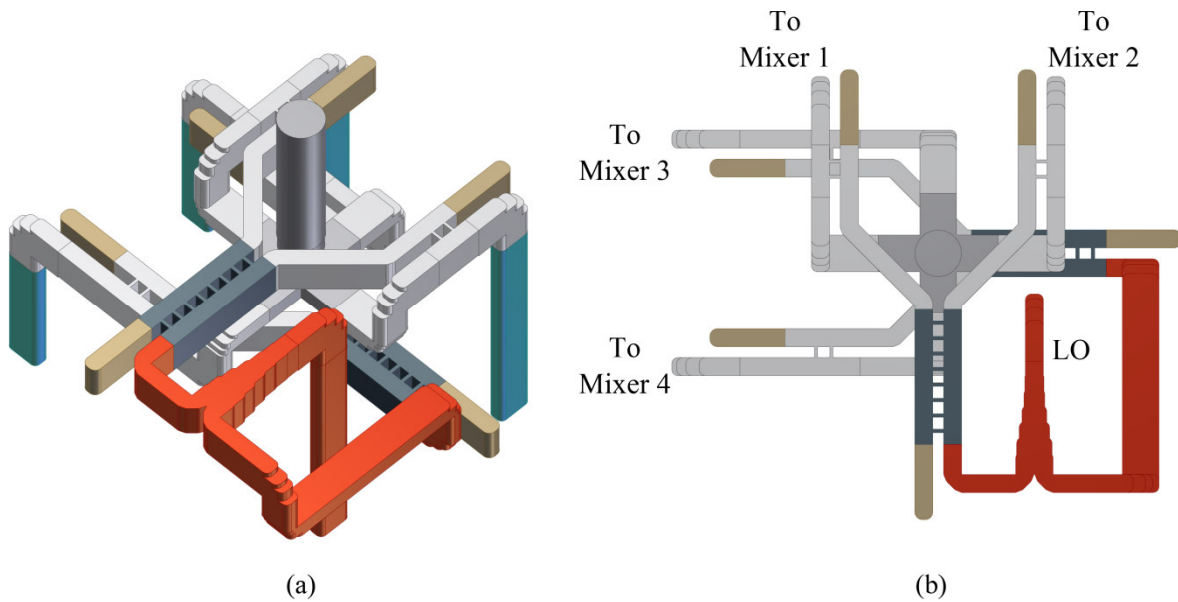


Fig. 21. Full 2SB assembly for both polarisations showing isometric (a) and top (b) views. Each dual-polarisation assembly has one LO input (shown in red) and four outputs that are routed to a separate housing for the mixers (not shown).

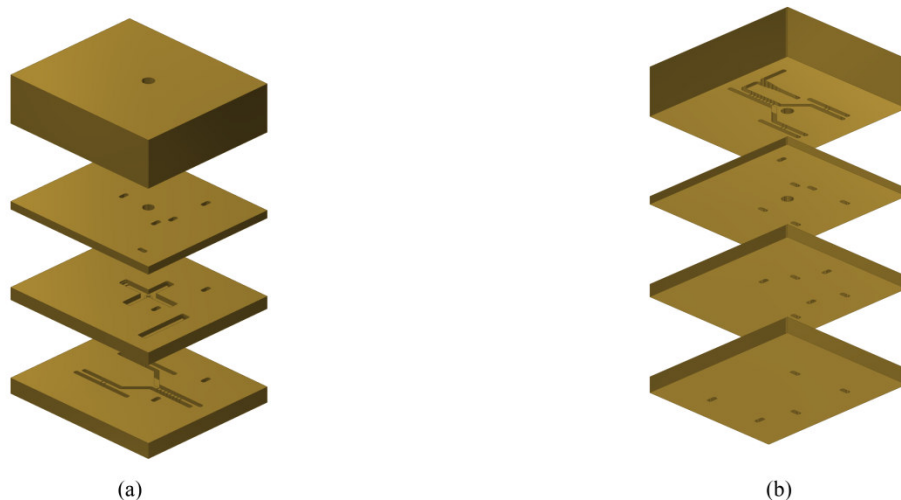


Fig. 22. Block implementation of the dual-linear polarisation, 2SB assembly for machining. The top two pieces may be machined from one side only, but the bottom two pieces require machining from both sides. Symmetric features are defined from one side only and high machining accuracy is preserved since features depend on the relative machine tolerance.

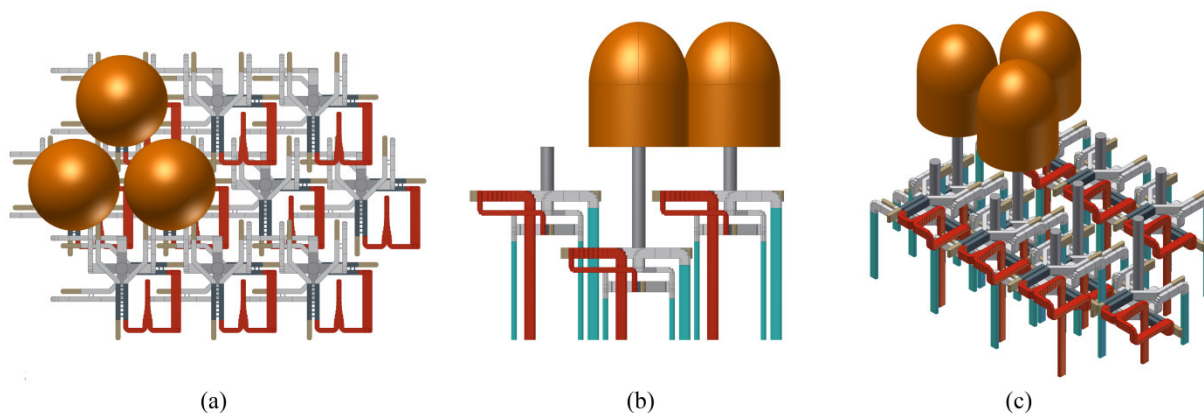


Fig. 23. Array implementation of the compact 2SB assembly. Every second row within the array may be offset to allow for a nested configuration of dual polarisation 2SB assemblies. The spacing corresponds with Fig. 19 (a) and elliptical lenses are shown for three of the inputs.

There are examples of very compact 2SB assemblies that could be suitable for closely packed arrays, such as a planar implementation in [32]. Other examples are [34]–[36] where the LO coupler has been combined on chip and a very compact superconducting IF coupler is used.

In [37], a “magic-T” has been used for the signal division required for 2SB. Similar to this, a turnstile can be used for the signal division with the added bonus that both linear polarisations can be captured. Previous work at NRC has included orthomode transducer (OMT) development using turnstiles [38], [39]. By integrating the OMT with the waveguide combiner network, the sideband separation assembly can be made very compact and symmetrical. Fig. 20 illustrates the integrated 2SB path for one of the polarisations and Fig. 21 shows the complete dual polarisation 2SB layout. The LO input, shown in red, is divided for input into each polarisation branch. Since the RF signal is split in-phase via the turnstile, each LO path contains a 3 dB hybrid to

make the LO outputs orthogonal before coupling into the RF signal path. The LO + RF signal is then routed to a separate block containing the mixers (this allows for separate mixer characterisation and matching for sideband separation).

Fig. 22 shows the design concept for machining. Similar to the W-Band OMTs [39], the block can be sectioned transverse to the circular waveguide input. Symmetric features of the block are completely defined within one surface and may be accurately machined since the tolerance of the feature is determined by the *relative* machining precision. In comparison to the OMTs, however, some of the pieces need to be machined from both sides, requiring an additional step in the machining process.

Finally, Fig. 23 describes how the compact 2SB assemblies may be stacked together to fit into the volume as determined by twice-Nyquist spacing shown in Fig. 19(a). Only three elliptical lenses are shown for clarity and illustrate the spacing achieved. Every second row within the array may be offset to create a nested configuration. As with any array, the number of outputs creates an increase in complexity and using the example of a 10 element array requires 10 LO signal inputs and 40 output channels. Note that the LO coupling into the signal path is completely defined by the waveguide couplers which avoids the need to quasi-optically combine the LO to the signal array. To preserve the compactness of the array, it is envisioned that a compact IF coupler, similar to that shown in [36], would be used within the mixer block.

Acknowledgment

The authors would like to acknowledge: J. Atwood and J. Pazder for interesting conversations about optics fundamentals; T. Hardy and J.-P. Veran for informative discussions of optical detectors; and Lewis Knee for helpful editing of this report.

This material is based upon work supported by Associated Universities, Inc./National Radio Astronomy Observatory and the National Science Foundation under Cooperative Agreement No. AST-0836064.

References

- [1] C. E. Groppi and J. H. Kawamura, "Coherent Detector Arrays for Terahertz Astrophysics Applications," *IEEE Trans. THz Sci. Technol.*, vol. 1, no. 1, pp. 85–96, Sept. 2011.
- [2] J. V. Buckle et al., "HARP/ACIS: a submillimetre spectral imaging system on the James Clerk Maxwell Telescope," *MNRAS*, vol. 399, no. 2, pp. 1026–1043, 2009.
- [3] K.-F. Schuster, C. Boucher, W. Brunswig, M. Carter, J.-Y. Chenu, B. Foulieux, A. Greve, D. John, B. Lazareff, S. Navarro, A. Perrigouard, J.-L. Pollet, A. Sievers, C. Thum, and H. Wiesemeyer, "A 230 GHz heterodyne receiver array for the IRAM 30 m telescope," *Astronomy and Astrophysics*, vol. 423, no. 3, pp. 1171–1177, Sept. 2004.
- [4] SEQUOIA: The Worlds' Fastest 3mm Imaging Array (2015, Mar.). [Online] Available: <http://www.astro.umass.edu/~fcrao/instrumentation/sequoia/seq.html>
- [5] T. Nakajima, K. Kimura, T. Katase, M. Koyano, H. Inoue, T. Sakai, H. Iwashita, C. Miyazawa, S. Asayama, N. Kuno, H. Ogawa, T. Onishi, R. Kawabe, and T. Noguchi, "Development of a New Multi-Beam Array 2SB Receiver in 100 GHz Band for the NRO 45-m Radio Telescope," in *Proc. 23rd Int. Symp. Space Terahertz Technol.*, Tokyo, Japan, Apr. 2–4.
- [6] C. Groppi, C. Walker, C. Kulesa, D. Golish, J. Klooster-man, S. Weinreb, G. Jones, J. Barden, H. Mani, T. Kuiper, J. Kooi, and A. Lichtenberger, "Testing and Integration of Supercam, a 64- Pixel Array Receiver for the 350 GHz Atmospheric Window," in *Proc. 21st Int. Symp. Space Terahertz Technol.*, Mar. 2010, pp. 368–373.
- [7] G. Anderson et al., "A 7-element K-Band focal plane array," (2015, Mar.). [Online] Available: http://www.radionet-eu.org/fp7wiki/lib/exe/fetch.php?media=na:engineering:ew:morgan_final.pdf
- [8] K. Devaraj, S. Church, K. Cleary, D. Frayer, R. Gawande, P. Goldsmith, J. Gundersen, A. Harris, P. Kangaslahti, A. C. S. Readhead, R. Reeves, L. Samoska, M. Sieth, and P. Voll, "Argus: A Scalable W-band 16-pixel focal plane array for the Green Bank Telescope," in *The Interstellar Medium in High Redshift Galaxies Comes of Age, NRAO Conference Series*, Vol. 28, 2012.
- [9] R. Gusten et al., "Submillimeter heterodyne arrays for APEX," in *Proc. SPIE 7020, Millimeter, Submillimeter, and Far-Infrared Detectors and Instrum. Astronomy IV*, vol. 7020, Aug. 2008, pp. 702010-1– 702010-12.

-
- [10] J. Yang et al., "The superconducting spectroscopic array receiver (SSAR): The next-generation molecular line instrument." in *2nd Chinese-German Workshop on Star & Planet Formation*, Jul. 27–30, 2010. [Online] Available: http://www.astrophysik.uni-kiel.de/~star/SinoGerman2010/Second_Chinese-German_Workshop_on_Star_and_Planet_Formation/Talks/SSAR4Sino-German%20Workshop2010.pdf
- [11] J. Yang 2014, private communication.
- [12] The CCAT Project (Mar. 2015). [Online] Available: http://www.ccatobservatory.org/docs/ccat-posters-brochures/AASposter2_2014Jan.pdf
- [13] J. Lesurf, *Millimetre-wave Optics, Devices and Systems*, England: IOP Publishing Ltd., 1990.
- [14] J. Murphy and R. Padman, "Focal-Plane and Aperture-Plane Heterodyne Array Receivers for Millimeter-Wave Radioastronomy—A Comparison," *Int. J. Infrared Millim. Waves*, vol. 9, no. 8, Aug. 1988.
- [15] P. F. Goldsmith, C.-T. Hsieh, G. R. Huguenin, J. Kapitzky, and E. L. Moore, "Focal plane imaging systems for millimeter wavelengths," *IEEE Trans. Microw. Theory Techn.*, vol. 41, no. 10, pp. 1664–1675, Oct. 1993.
- [16] C. A. Balanis, *Antenna Theory: Analysis and Design*, 2nd ed., New York: John Wiley & Sons, Inc., 1997.
- [17] J. F. Johansson, "Fundamental limits for focal-plane array efficiency," in *Proc. Multi-Feed Systems for Radio Telescopes, ASP Conf.*, vol. 75, pp. 34–41, 1995.
- [18] A. Lundgren, "ALMA Cycle 2 Technical Handbook", ver. 1.1, 2013. <http://www.almascience.org>.
- [19] P. F. Goldsmith, "Focal plane arrays for millimeter-wavelength astronomy," in *IEEE MTT-S Int. Microw. Symp. Dig.*, vol. 3, pp.1255–1258, Jun. 1992.
- [20] J. W. Lamb, "Low-noise, high-efficiency optics design for ALMA receivers," *IEEE Trans. Antennas Propag.*, vol. 51, no. 8, pp. 2035–2047, Aug. 2003.
- [21] R. Padman, "Optical fundamentals for array feeds," in *Proc. Multi-Feed Systems for Radio Telescopes, ASP Conf.*, vol. 75, pp. 3–26, 1995.
- [22] R. Padman, J. A. Murphy, and R. E. Hills, "Gaussian mode analysis of Cassegrain antenna efficiency," *IEEE Trans. Antennas Propag.*, vol. AP-35, pp. 1093–1103, Oct. 1987.
- [23] P. F. Goldsmith, *Quasioptical Systems: Gaussian Beam Quasioptical Propagation and Applications*. New York: IEEE Press, 1998.
- [24] J. Glenn, P. Ade, M. Amarie, J. Bock, S. Edgington, A. Goldin, S. Golwala, D. Haig, A. Lange, G. Laurent, P. Mauskopf, M. Yun, and H. Nguyen, "Current status of Bolocam: a large-format millimeter-wave bolometer camera," in *Proc. SPIE 4855, Millim. Submillim. Detectors Astron.*, vol. 4855, no. 30, Feb. 2003.
- [25] B. Weiner. (2008, Sept.). Scaling relations for telescopes, spectrographs, and reimaging instruments. Stewart Observatory, University of Arizona, Tucson, Arizona. [Online]. Available: <http://mingus.as.arizona.edu/~bjw/spectrographs/spectrographs.pdf>
- [26] M. Carter, et al., "ALMA front-end optics design report," Nat. Radio Astron. Observatory, Charlottesville, VA, ALMA EDM Doc. FEND-40.02.00.00-035-B-REP, Jul. 2007.
- [27] D. F. Filipovic, S. S. Gearhart, G. M. Rebeiz, "Double-slot antennas on extended hemispherical and elliptical silicon dielectric lenses," *IEEE Trans. Microw. Theory Techn.*, vol. 41, no. 10, pp. 1738–1749, Oct. 1993.
- [28] K. Pontoppidan, "Electromagnetic properties and optical analysis of the ALMA antennas and front ends," Nat. Radio Astron. Observatory, Charlottesville, VA, ALMA EDM Doc. FEND-80.04.00.00-026-A-REP, Jan. 2008.
- [29] S. Claude, P. Niranjana, F. Jiang, D. Duncan, D. Garcia, M. Halman, H. Ma, I. Wevers, and K. Yeung, "Performance of the production band 3 receivers (84–116 GHz) for the Atacama Large Millimeter Array (ALMA)," *Int. J. Infrared Millim. Waves*, vol. 35, no. 6-7, pp. 563–582, Jul. 2014.
- [30] B. Veidt, T. Burgess, K. Yeung, S. Claude, I. Wevers, M. Halman, P. Niranjana, C. Yao, A. Jew, D. Henke, and A. G. Willis, "Noise performance of a phased-array feed composed of thick Vivaldi elements with embedded low-noise amplifiers," in *Proc. 9th European Conf. Antennas Propag.*, 2015, to be presented.
- [31] A. R. Kerr, S.-K. Pan, S. M. X. Claude, P. Dindo, A. W. Lichtenberger, J. E. Effland, and E. F. Lauria, "Development of the ALMA Band-3 and Band-6 Sideband-Separating SIS Mixers," *IEEE Trans. THz Sci. Technol.*, vol. 4, no. 2, pp. 201–212, Mar. 2014.
- [32] A. R. Kerr and S.-K. Pan, "Design of planar image-separating and balanced SIS mixers," in *Proc. 7th Int. Symp. Space Terahertz Technol.*, Mar. 12–14, 1996, pp. 207–219.
- [33] S. M. X. Claude, C. T. Cunningham, A. R. Kerr, and S.-K. Pan, "Design of a sideband-separating balanced SIS mixer based on waveguide hybrids, ALMA Memo No. 316, 2000.
- [34] R. Monje, V. Belitsky, C. Risacher, V. Vassilev, and A. Pavolotsky, "SIS mixer for 385–500 GHz with on chip LO injection," in *Proc. 18th Int. Symp. on Space Terahertz Technol.*, Mar. 2007, pp. 44–49.
- [35] V. Vassilev, D. Henke, I. Lapkin, O. Nystrom, R. Monje, A. Pavolotsky, V. Belitsky, "Design and Characterization of a 211–275 GHz Sideband Separating Mixer for the APEX Telescope," *Microw. Wireless Comp. Lett.*, vol. 18, no. 1, pp. 58–60, Jan. 2008.
- [36] B. Billade, O. Nystrom, D. Meledin, E. Sundin, I. Lapkin, M. Fredrixon, V. Desmaris, H. Rashid, M. Strandberg, S.-E. Ferm, A. Pavolotsky, and V. Belitsky, "Performance of the First ALMA Band 5 Production Cartridge," *IEEE Trans. THz Sci. Technol.*, vol. 2, no. 2, pp. 208–214, Mar. 2012.
- [37] R. Akeson, J. Carlstrom, D. Woody, J. Kawamura, A. Kerr, S.-K. Pan, and K. Wan, "Development of a sideband separation receiver at 100 GHz," in *Proc. 4th Int. Symp. on Space Terahertz Technol.*, Los Angeles, CA, Mar. 1993, pp. 12–17.
- [38] D. Henke and S. Claude, "Minimizing RF Performance Spikes in a Cryogenic Orthomode Transducer (OMT)," *IEEE Trans. Microw. Theory Techn.*, vol. 62, no. 4, pp. 840–850, Apr. 2014.
- [39] D. Henke and S. Claude, "Design of a 70–116 GHz W-band turnstile OMT," in *44th Eur. Microw. Conf.*, Rome, Italy, Oct. 6–9, 2014, pp. 456–459.